STATE OF CALIFORNIA DEPARTMENT OF TRANSPORTATION

TECHNICAL REPORT DOCUMENTATION PAGE

TR0003 (REV. 10/98)

1. REPORT NUMBER	2. GOVERNMENT ASSOCIATION NUMBER	3. RECIPIENT'S CATALOG NUMBER
CA18-2881		

4. TITLE AND SUBTITLE	5. REPORT DATE
Next-Gen Monitoring and Evaluation of California Bridges	December 2018
	6. PERFORMING ORGANIZATION CODE ISU

7. AUTHOR(S)	8. PERFORMING ORGANIZATION REPORT NO.
Alipour Alice, Laflamme Simon, Sritharan Sri, Alessandro Cancelli, Kanta Prajapat	ISU / CA18-2881

9. PERFORMING ORGANIZATION NAME AND ADDRESS	10. WORK UNIT NUMBER
Department of Civil and Environmental Engineering Iowa State University, Ames IA 50011	11. CONTRACT OR GRANT NUMBER 65A0586

12. SPONSORING AGENCY AND ADDRESS	13. TYPE OF REPORT AND PERIOD COVERED
California Department of Transportation Engineering Service Center 1801 30th Street, MS 9-2/5i Sacramento, California 95816	Final Report 2/1/2016 – 11/30/2017 14. SPONSORING AGENCY CODE
California Department of Transportation Division of Research and Innovation, MS-83 1727 30th Street, 2nd Floor Sacramento CA 95816	913

15. SUPPLEMENTAL NOTES

Prepared in cooperation with the State of California Department of Transportation.

16. ABSTRACT

The problem of aging structures is becoming a dominant issue in management of infrastructure systems. Among all the structures, aging of bridges is one of the predominant issue as often times bridges act as bottle necks for the highway systems. This underlines importance of techniques that allow for identification of damage to the bridge at early stages and provide the means for informed planning. Traditional inspection methods such as visual inspection have been in use by the transportation agencies but have shown to be costly. The methods are subjective in nature and rely on the human factors of the inspectors. Furthermore, they require the presence of the inspector at the location of the bride which may not be feasible due to lack of resources and skilled inspectors. An important step forward for the bridge safety could be the use of available structural health monitoring (SHM) data to assess the state of the structure.

This underlines the necessity to develop a robust method to identify, locate and quantify the damage on the structure using data collected from a network of sensors under normal loading condition (ambient vibration caused by traffic loading on the bridge), allowing for real time safety assessment of the bridge condition. This report will focus on the experimental activity conducted on a girder set up that represent a segment of the bridge. The set up involves a partial girder-deck system, tested under three different level of structural damage. The experimental set ups were used for the validation of the new damage detection and quantification techniques. A set of both deterministic and Bayesian approaches were implemented to assess the level of damage.

17. KEY WORDS	18. DISTRIBUTION STATEMENT	
System Identification, Non-Destructive Damage Detection, Estimation of Damage Entity, Bayesian updating, Estimation of Structural Properties	No restrictions. This document is available to the public through the National Technical Information Service, Springfield, VA 22161	
19. SECURITY CLASSIFICATION (of this report)	20. NUMBER OF PAGES	21. PRICE
Unclassified	82	

DISCLAIMER STATEMENT

This document is disseminated in the interest of information exchange. The contents of this report reflect the views of the authors who are responsible for the facts and accuracy of the data presented herein. The contents do not necessarily reflect the official views or policies of the State of California or the Federal Highway Administration. This publication does not constitute a standard, specification or regulation. This report does not constitute an endorsement by the Department of any product described herein.

For individuals with sensory disabilities, this document is available in Braille, large print, audiocassette, or compact disk. To obtain a copy of this document in one of these alternate formats, please contact: the Division of Research and Innovation, MS-83, California Department of Transportation, P.O. Box 942873, Sacramento, CA 94273-0001.

STRUCTURAL HEALTH MONITORING (SHM) FOR EVALUATION OF STRUCTURAL INTEGRITY

Final Report
December 2018

Principal Investigator
Alice Alipour, Ph.D., P.E.
Department of Civil, Construction and Environmental Engineering

Co-Principal Investigators
Sri Sritharan, Ph.D., Professor
Simon Laflamme, Ph.D., Associate Professor.

Research Assistants
Alessandro Cancelli and Kanta Prajapat

Authors
Alice Alipour, Sri Sritharan, Simon LaFlamme,
Alessandro Cancelli, Kanta Prajapat

Final Report Submitted to
the California Department of Transportation under Contract No. 65A0586
Report No. CA18-2881

Iowa State University
Department of Civil Construction and Environmental Engineering

Note: The report contains material previously published in: Cancelli, A., Laflamme, S., Alipour, A., Sritharan, S., and Ubertini, F. (2018), “Vibration-based damage localization and quantification in a pretensioned concrete girder using stochastic subspace identification and particle swarm model updating”, Structural Health Monitoring, X(XX), 2-31.

TABLE OF CONTENTS

LIST OF FIGURES

LIST OF TABLES

ACKNOWLEDGMENTS

This project was supported by California Department of Transportation division of research and innovation. The authors would like to acknowledge the support from Caltrans. The research team would like to extend special appreciation to California Department of Transportation for funding this project.

EXECUTIVE SUMMARY

Despite the decades of research and development in the field of structural health monitoring and system identification, there is currently no definitive approach for reliability analysis of the structures based on the measured data. Caltrans has been one of the leading agencies in deploying health monitoring devices such as accelerometers, strain gages, and anemometers to monitor the bridges in the state of California. The wealth of knowledge collected from such dense instrumentation has helped advance the design and retrofit decisions, especially under extreme events such as earthquakes and windstorms, over the years. However one of the greatest potentials of the collected data has remained untapped; that is the capability to use the data for real-time or near-real-time assessment of the state of the bridges under service loads.

This report provides a damage identification and a reliable Bayesian-based updating scheme that would update structural characteristics based on the sensed data. The goal is to be able to use these methodologies to assess the remaining life capacity of the structures. In pursuing the study laboratory tests were conducted in controlled environments to calibrate the sensors and validate the applicability of the developed framework. Specific tools for system identification were developed so as to satisfy physically meaningful optimality conditions.

The following main objectives have been achieved in this project:

1. A reliable signal processing approach, considering the effects of environmental conditions, and system identification methodology that would result in damage localization
2. Two sets of controlled and scaled experiments developed for validation of the computational models
3. A detailed FE model of the structure in a commercial package selected by Caltrans and Bayesian-based approach to update the mathematical model of the structure based on the data collected from sensors

The report consists of eight major chapters in addition to introduction and conclusions and future work chapters.

CHAPTER 1: INTRODUCTION

1.1 Problem presentation and research objective

Condition-based maintenance of transportation infrastructures is emerging as a cost-effective solution to allocate limited resources to the aging infrastructure problem. Unlike traditional breakdown-based and time-based strategies [1], condition-based maintenance has the potential to decrease costs from the improved efficiency of maintenance and repair decision [2]. This requires knowledge of structural conditions that are typically evaluated through visual inspection, which is a process known to be lengthy, costly and subjective. An alternative is to automate the inspection process through structural health monitoring (SHM) methods. SHM generally consists of collecting, processing and interpreting a continuous set of data measured from a set of sensors installed on a structure to diagnose, localize and prognose the extent of damage, and/or evaluate and forecast structural conditions based on the retrieved information. A challenge in deploying SHM solutions to civil structures and structural members is in the large geometries under consideration, whereas sensors need to be strategically deployed in order to provide rich-enough data that can yield to condition-based information[3]. This can be done using sparse [4] and dense [5] networks of sensors measuring strain [6], [7], acceleration [8]–[11], and other [12]–[14] states.

Acceleration-based SHM solutions have shown promise due to the possibility of retrieving global modal information from a structure. This vibration-based method generally consists of associating damage with changes in modal properties [15]. Operational modal analysis (OMA) [16] using stochastic subspace identification (SSID) is a suitable choice due to the capability of identifying structural modal properties using only the measured structural response without the knowledge of input data (a very likely scenario in case of bridges). A notable advantage of SSID-based methods is their suitability for automated implementations [17]–[21], making them a powerful tool for SHM purposes. SSID can be conducted through either covariance-driven (SSID-COV) [22] or data driven (SSID-DATA) algorithms. SSID-DATA is of particular interest, because modal parameters can be identified directly from the measured time signal, unlike the SSID-COV where one needs to obtain the covariance matrix relating all of the measured system outputs. An exhaustive summary on these methods and their applications to civil engineering structures can be found in [23]–[28]. Many applications of SSID have been proposed and demonstrated. For instance Peeters et al. [29] proposed the combination of SSID and auto-regressive exogenous (ARX)

methods for damage detection applied to the Z24 Bridge benchmark case study. Acceleration data from the Z24 Bridge were analyzed using SSID to obtain the evolution of the first four modes as a function of wearing surface temperature. Subsequently, an ARX model was used to relate temperature to frequencies and produce a predictive model. The prediction error data was then used as the damage detection feature. Also using the Z24 Bridge benchmark, Kullaa [30] proposed a damage detection approach combining SSID and statistical control charts. SSID was used to retrieve the structural modal properties under different damage conditions. The information was grouped using mode pairing based on a minimal Euclidean distance criteria. The grouped modal properties were then used to construct statistical control charts, whose bounds were used as the damage detection feature.

Outside the Z24 benchmark, Su et al. [31] proposed a damage detection method for multi-story frame buildings based on the combination of the SSID and the Gram-Schmidt orthogonalization process. Acceleration data collected under earthquake excitation were analyzed through a wavelet-based SSID approach to identify frequencies and mode shapes. Mode shapes were mass-normalized and corrected using the Gram-Schmidt orthogonalization process, followed by the construction of a diagonal modal stiffness matrix used for damage detection. Similar to other OMA and vibration-based SHM methods, several sources of uncertainty such as material properties, non-white noise and non-stationary loading, as well as changes in environmental and operational conditions, may affect the performance of the algorithm to relate changes in modal properties to damage. A solution to overcome this challenge is to treat the damage identification task as an optimization problem. Using this strategy, the identified modal properties are used in combination with a structural model to build specific optimization functions. Optimization algorithms are used to minimize the error in the dynamic properties of the model with respect to the real structure, enabling accurate damage location and quantification [32], [33]. Popular algorithms include the metaheuristics approaches (e.g., particle swarm optimization (PSO), firefly algorithms) [34]–[38], hybridized metaheuristics approaches (e.g., PSO/simplex algorithm) [39], [40] and stochastic/deterministic methods (e.g., Nelder-Mead methods) [34, 15]. In particular, Meruane and Heylen [41] proposed a combination of SSID with a genetic algorithm where SSID was used to retrieve the system's modal properties, which were then combined with a structural model to build optimization functions. A genetic algorithm was used to perform the optimization, yielding localization and quantification of damage.

The methods proposed in this study combines SSID with an optimization algorithm, while integrating a model reduction method to reconstruct a higher resolution finite element model (FEM) of the monitored structure. More in detail, it consists of extracting modal information, including modal frequencies and shapes, using an SSID algorithm. Subsequently, a reduced order stiffness matrix is reconstructed based on the system equivalent reduction expansion process (SEREP) [42]. At the final stage, a FEM is reconstructed and updated by optimizing three newly developed optimization functions. The approach selected for the optimization purpose in this study was a particle swarm optimization (PSO) algorithm [43], [44], due to its flexibility and ease of implementation. It must be noted that other optimization strategies could have been utilized. The PSO performed the optimization of the three different functions, and this result was used to achieve damage localization and quantification. The damage detection capabilities of the framework were verified using simulation and experimental data. First, simulation of a simply supported reinforced concrete (RC) beam and of a system composed of two RC girders connected by a deck were used to validate the capabilities and limitations of the proposed approach. Then, the proposed method is validated using experimental data obtained from a full scale experiment. The experiments involved the analysis of a full-scale pretensioned concrete (PC) girder under three different damage scenarios. Such a system was subjected to progressively increasing damage, starting from the incipient damage condition (formation of first crack) to the near collapse condition.

1.2 Report roadmap

The present report will present all the results obtained from the simulation and experimental activities of the project, highlighting the capability of the algorithm in all the tested scenarios.

Chapter 2 will introduce the theoretical background needed to understand the working principle of the damage detection algorithm.

Chapter 3 will present the characteristic of the instrumentation used for the data acquisition and the excitation in both the experimental test.

Chapter 4 will detail the functions and algorithms that describe the damage detection algorithm.

Chapter 5 will show the performance of the proposed method in different simulated scenarios.

Chapter 6 presents the experimental tests and the result obtained with the proposed algorithm in terms of location and quantification of structural damage.

Chapter 7 will briefly introduce how the damage detection results can be implemented in a framework to predict future damage states of structural systems

Chapter 8 will discuss the fundamentals of Bayesian approaches and presents the strength of the methodology in the context of experimental plans discussed

Chapter 9 will conclude the study, highlighting the achieved results and indicating possible future research paths.

CHAPTER 2: THEORETICAL BACKGROUND

The proposed damage identification and quantification technique leverages the SSID, SEREP, and PSO algorithms. This section summarizes the theoretical background for each of these methods.

2.1 Stochastic subspace identification

SSID is a dynamic analysis tool that is generally used for retrieving natural frequencies, mode shapes and modal damping from output-only data. Dynamic properties are obtained through a linear state-space representation reconstructed directly from measured data. Consider the discrete-time state space representation of a linear time-invariant dynamical system [45]:

$$\begin{aligned} \mathbf{x}_{k+1} &= \mathbf{A}\,\mathbf{x}_k + \mathbf{w}_k \\ \mathbf{y}_k &= \mathbf{C}\,\mathbf{x}_k + \mathbf{v}_k \end{aligned} \tag{2-1}$$

where the subscript k indicates a discrete step; $\mathbf{x}$ is the state vector; $\mathbf{A}$ is the state matrix; $\mathbf{y}$ is the output vector; $\mathbf{C}$ is the output matrix; $\mathbf{w}$ and $\mathbf{v}$ are zero-mean Gaussian stationary processes representing process and excitation noise, respectively. Both Gaussian processes are defined by their covariance matrix $\mathbf{\Sigma}$:

$$\mathbf{\Sigma} = \begin{bmatrix} \mathbf{L}_w & \mathbf{S}_{w,v} \\ \mathbf{S}_{w,v}^{\mathrm{T}} & \mathbf{Z}_v \end{bmatrix} \tag{2-2}$$

where $\mathbf{L}_w$ is the variance matrix of $\mathbf{w}$; $\mathbf{Z}_v$ is the variance matrix of $\mathbf{v}$, and $\mathbf{S}_{w,v}$ is the covariance matrix between both Gaussian processes.

To conduct the SSID-DATA procedure [22] a block Henkel matrix, $\mathbf{H}$, is first constructed from the measured data. The dimension of this matrix depends on two user-defined quantities $2i$ and j, which represent the matrix's number of output row blocks and columns, respectively.

$$\mathbf{H}_i = \left[\begin{array}{cccc} y(0) & y(1) & \cdots & y(j-1) \\ y(1) & y(2) & \cdots & y(j) \\ \vdots & \vdots & \ddots & \vdots \\ y(i-1) & y(i) & \cdots & y(i+j-2) \\ \hline y(i) & y(i+1) & \cdots & y(i+j-1) \\ y(i+1) & y(i+2) & \cdots & y(i+j) \\ \vdots & \vdots & \ddots & \vdots \\ y(2i-1) & y(2i) & \cdots & y(2i+j-2) \end{array}\right] = \left[\begin{array}{c} \mathbf{Y}_p \\ \hline \mathbf{Y}_f \end{array}\right] \tag{2-3}$$

Matrix $\mathbf{H}$ is subdivided into submatrices $\mathbf{Y}_p$ and $\mathbf{Y}_f$, usually termed past and future output block matrices. Both submatrices have i block rows and j columns, with $j \leq s-2i+1$ and s is the total number of time samples available. The block Henkel matrix is decomposed using the QR-factorization:

$$\mathbf{H}_i = \begin{bmatrix} \mathbf{Y}_p \\ \mathbf{Y}_f \end{bmatrix} = \mathbf{R}\mathbf{Q}^{\mathrm{T}} \tag{2-4}$$

where $\mathbf{Q}$ is a square orthonormal matrix of dimension j such that $\mathbf{Q}^{\mathrm{T}}\mathbf{Q} = \mathbf{Q}\mathbf{Q}^{\mathrm{T}} = \mathbf{I}_j$ with $\mathbf{I}_j$ being the identity matrix of dimension j, and $\mathbf{R}$ is a lower triangular matrix of dimension $k \times j$ with k being the total number of sensors. Using the decomposition of the Henkel matrix, the orthogonal projection $\mathbf{P}_i$ of the past row space into the future row space is computed as:

$$\mathbf{P}_i = \mathbf{Y}_f / \mathbf{Y}_p = \mathbf{Y}_f \mathbf{Y}_p^{\mathrm{T}} \left(\mathbf{Y}_p \mathbf{Y}_p^{\mathrm{T}} \right)^{\dagger} \mathbf{Y}_p = \begin{bmatrix} \mathbf{R}_{21} \\ \mathbf{R}_{31} \\ \mathbf{R}_{41} \end{bmatrix} \mathbf{Q}_1^{\mathrm{T}} \tag{2-5}$$

where $(\bullet)^{\dagger}$ is the Moore-Penrose pseudo-inverse, $\mathbf{R}_{21}$, $\mathbf{R}_{31}$, $\mathbf{R}_{41}$ are submatrices of $\mathbf{R}$, and $\mathbf{Q}_1$ is a submatrix of $\mathbf{Q}$. The projection is expressed as a product between the observability matrix of the system $\mathbf{O}_i$ and a Kalman filter state sequence $\hat{\mathbf{X}}_i$:

$$\mathbf{P}_i = \begin{bmatrix} \mathbf{C} \\ \mathbf{C}\mathbf{A} \\ \mathbf{C}\mathbf{A}^2 \\ \cdots \\ \mathbf{C}\mathbf{A}^{i-1} \end{bmatrix} \begin{bmatrix} \hat{\mathbf{x}}_i & \hat{\mathbf{x}}_{i+1} & \cdots & \hat{\mathbf{x}}_{i+j-1} \end{bmatrix} = \mathbf{O}_i \hat{\mathbf{X}}_i \tag{2-6}$$

Both $\mathbf{O}_i$ and $\hat{\mathbf{X}}_i$ are retrieved through the singular value decomposition (SVD) of the projection as follows:

$$\mathbf{P}_i = \mathbf{U}\mathbf{S}\mathbf{V}^{\mathrm{T}} \tag{2-7}$$

$$\mathbf{O}_i = \mathbf{U}\mathbf{S}^{1/2} \tag{2-8}$$

$$\hat{\mathbf{X}}_i = \mathbf{O}_i^{\dagger} \mathbf{P}_i \tag{2-9}$$

where $\mathbf{U}$, $\mathbf{S}$ and $\mathbf{V}$ are the matrices obtained from the SVD. An overdetermined set of linear equations is obtained from the estimated Kalman filter state sequence as follows:

$$\begin{bmatrix} \hat{\mathbf{X}}_{i+1} \\ \mathbf{Y}_i \end{bmatrix} = \begin{bmatrix} \mathbf{A} \\ \mathbf{C} \end{bmatrix} \hat{\mathbf{X}}_i + \begin{pmatrix} \boldsymbol{\rho}_w \\ \boldsymbol{\rho}_v \end{pmatrix} \tag{2-10}$$

where $\mathbf{Y}_i$ is an Henkel matrix with only one row block, while $\boldsymbol{\rho}_w$ and $\boldsymbol{\rho}_v$ are the residuals of the modelling and data noise, respectively. Solving this overdetermined problem by a least square approach yields matrices **A** and **C** in a discrete-time form:

$$\begin{bmatrix}\mathbf{A}\\ \mathbf{C}\end{bmatrix}=\begin{bmatrix}\hat{\mathbf{X}}_{i+1}\\ \mathbf{Y}_i\end{bmatrix}\hat{\mathbf{X}}_i^{\dagger} \tag{2-11}$$

The retrieved **A** matrix can be decomposed using its eigenvalues and eigenvectors yielding:

$$\mathbf{A}=\boldsymbol{\Psi}_d\boldsymbol{\Lambda}_d\boldsymbol{\Psi}_d^{-1} \tag{2-12}$$

$$\boldsymbol{\Lambda}_d=\begin{bmatrix}\lambda_{d,1} & 0 & \cdots & 0\\ 0 & \lambda_{d,2} & \cdots & 0\\ \vdots & \vdots & \ddots & \vdots\\ 0 & 0 & \cdots & \lambda_{d,n}\end{bmatrix} \tag{2-13}$$

where $\boldsymbol{\Lambda}_d$ is a diagonal matrix containing the $\lambda_{d,1}$, $\lambda_{d,2}$, …, $\lambda_{d,n}$ discrete time complex eigenvalues and $\boldsymbol{\Psi}_d$ is the discrete time complex eigenvector matrix. These discrete time quantities need to be converted into continuous time quantities to obtain the dynamic parameters of the system:

$$\mathbf{A}=e^{\mathbf{A}_c\Delta t} \tag{2-14}$$

$$\mathbf{C}_c=\mathbf{C} \tag{2-15}$$

$$\lambda_c=\frac{\ln(\lambda_d)}{\Delta t} \tag{2-16}$$

$$\boldsymbol{\Psi}_c=\boldsymbol{\Psi}_d \tag{2-17}$$

where the subscript *d* indicates discrete-time quantities, the subscript *c* indicates continuous time quantities, λ is a vector containing the complex eigenvalues and Δt is the time step of the measured data. The circular frequencies ω_i and modal damping ξ_i of the system can be determined using the complex conjugates eigenvalues of the matrix $\mathbf{A}_c$:

$$\lambda_{c,i},\lambda_{c,i}^{*}=-\xi_i\omega_i\pm \mathrm{j}\,\omega_i\sqrt{1-\xi_i^2} \tag{2-18}$$

where the superscript * indicates the complex conjugate and *j* is the imaginary unit. Lastly, the mode shapes matrix $\boldsymbol{\Phi}$ of the system can be obtained from the continuous time eigenvectors $\boldsymbol{\Psi}_d$ as:

$$\boldsymbol{\Phi}=\mathbf{C}_c\boldsymbol{\Psi}_c \tag{2-19}$$

It follows that the dynamic properties of the structural system can be derived from the retrieved discrete-time matrices **A** and **C**.

In the SSID theory the order of the system n, or the dimension of the aforementioned matrices **A** and **C**, should be equal to twice the number of modes needed to accurately describe the structural response. However, when analyzing full-scale structures, a higher value of n is often required, to account for the possible presence of weakly excited and/or closely spaced modes. This over-modelling approach has the drawback of creating spurious modes associated with the measurements noise. To overcome this problem it has become common practice in the SSID analysis to evaluate the dynamic properties of the system over a wide range of n and i values. For the purpose of automating the separation of physical modes from the spurious ones, Ubertini et al. [20] developed a three-step automated modal identification procedure. First, the complex conjugates eigenvalues are eliminated from the results. Then, specific control criteria for frequencies, damping, and mode shapes are used to eliminate modes created from the noise in the identification process and from over-modelling. Finally, the remaining modes are clustered and the structure's modal information are selected by analyzing the stability of these modes through the similarity of the parameters in the various model's orders and number of output block rows of the block Henkel matrix.

2.2 System equivalent reduction expansion process condensation method

In the proposed method, the physical system is simplified into a finite element model of degrees-of-freedom (DOFs) equal to the number of sensors. This yields a reduced order model, dynamic properties of which can be obtained from the SSID method. A condensation technique is utilized to maintain equivalence between the dynamic properties of the full and reduced models, consisting of the SEREP [42]. This method is used for dynamic condensation and allows for the temporal comparison of dynamic properties, leading to the quantification of changes in stiffness. A specific performance matrix is created from this method in order to improve the precision of the reconstructed stiffness of the system. To derive the expression of the SEREP reduced order stiffness matrix, $\overline{\mathbf{K}}_{red,S}$, consider the following matrix form of the equation of motion [45]:

$$\mathbf{M}\,\ddot{\mathbf{x}} + \mathbf{C}_d\,\dot{\mathbf{x}} + \mathbf{K}\,\mathbf{x} = \mathbf{F}(t) \tag{2-20}$$

where $\mathbf{M}$ is the mass matrix, $\mathbf{C}_d$ is the damping matrix, $\mathbf{K}$ is the stiffness matrix, $\mathbf{F}(t)$ is forcing matrix, $\mathbf{x}$ is the displacement vector, and the dot denotes a time derivative. Eq. (2-20) can be divided in terms associated with the measured DOFs, m, and the complementary DOFs, c:

$$\begin{bmatrix} \mathbf{M}_{mm} \mathbf{M}_{mc} \\ \mathbf{M}_{cm} \mathbf{M}_{cc} \end{bmatrix} \begin{bmatrix} \ddot{\mathbf{x}}_m \\ \ddot{\mathbf{x}}_c \end{bmatrix} + \begin{bmatrix} \mathbf{C}_{d,mm} \mathbf{C}_{d,mc} \\ \mathbf{C}_{d,cm} \mathbf{C}_{d,cc} \end{bmatrix} \begin{bmatrix} \dot{\mathbf{x}}_m \\ \dot{\mathbf{x}}_c \end{bmatrix} + \begin{bmatrix} \mathbf{K}_{mm} \mathbf{K}_{mc} \\ \mathbf{K}_{cm} \mathbf{K}_{cc} \end{bmatrix} \begin{bmatrix} \mathbf{x}_m \\ \mathbf{x}_c \end{bmatrix} = \begin{bmatrix} \mathbf{F}_m(t) \\ \mathbf{F}_c(t) \end{bmatrix} \tag{2-21}$$

To correlate the above equations with the retrieved dynamic properties of the system, a coordinate change is introduced as:

$$\mathbf{x}(t) = \begin{bmatrix} \mathbf{x}_m(t) \\ \mathbf{x}_c(t) \end{bmatrix} = \mathbf{\Phi}\, \mathbf{q}(t) = \begin{bmatrix} \mathbf{\Phi}_m \\ \mathbf{\Phi}_c \end{bmatrix} \mathbf{q}(t) \tag{2-22}$$

where $\mathbf{x}$ and $\mathbf{q}$ are associated with the physical and modal coordinates of the system, respectively, $\mathbf{\Phi}_m$ is a matrix containing the eigenvectors of the measured DOFs and $\mathbf{\Phi}_c$ is a matrix containing the eigenvectors of the complementary DOFs. If $\mathbf{\Phi}_m$ is known, it is possible to derive an expression from Eq. (2-22) representing the modal coordinates using a least square estimator:

$$\mathbf{q} = \mathbf{\Phi}_m^{\dagger} \mathbf{x}_m \tag{2-23}$$

Substituting (2-23) into (2-22) yields the transformation matrix for the SEREP approach:

$$\mathbf{x} = \mathbf{\Phi}\, \mathbf{\Phi}_m^{\dagger}\, \mathbf{x}_m = \mathbf{T}_r \mathbf{x}_m \tag{2-24}$$

$$\mathbf{T}_r = \mathbf{\Phi}\, \mathbf{\Phi}_m^{\dagger} \tag{2-25}$$

Using Eq. (2-24) in (2-20) and pre-multiplying by $\mathbf{T}_r^{\mathrm{T}}$ leads to:

$$\mathbf{T}_r^{\mathrm{T}} \mathbf{M}\, \mathbf{T}_r \ddot{\mathbf{x}}_m + \mathbf{T}_r^{\mathrm{T}} \mathbf{C}\, \mathbf{T}_r \dot{\mathbf{x}}_m + \mathbf{T}_r^{\mathrm{T}} \mathbf{K}\, \mathbf{T}_r \mathbf{x}_m = \mathbf{T}_r^{\mathrm{T}} \mathbf{F}(t) \tag{2-26}$$

Expanding the term of the equation relative to the stiffness matrix and noting that $\mathbf{\Phi}^{\mathrm{T}} \mathbf{K} \mathbf{\Phi} = \mathbf{\Omega}^2$, one obtains an expression for $\bar{\mathbf{K}}_{\mathrm{red,S}}$:

$$\bar{\mathbf{K}}_{\mathrm{red,S}} = \mathbf{T}_r^{\mathrm{T}} \mathbf{K}\, \mathbf{T}_r = \left(\mathbf{\Phi}_m^{\dagger}\right)^{\mathrm{T}} \mathbf{\Phi}^{\mathrm{T}} \mathbf{K}\, \mathbf{\Phi}\, \mathbf{\Phi}_m^{\dagger} = \left(\mathbf{\Phi}_m^{\dagger}\right)^{\mathrm{T}} \mathbf{\Omega}^2 \mathbf{\Phi}_m^{\dagger} \tag{2-27}$$

This condensation method preserves the selected eigenvalues of the original system through the transformation, implying that the selected mode's eigenvalues are equal for both systems. This property is independent of the location and the number of sensors.

2.3 Particle swarm optimization algorithm

The PSO is a probabilistic search algorithm used for optimization problems. It is based on a simplified social model derived from the behavior of animal swarms such as bees [43], [44]. Using

this approach, variables are optimized within a set of possible solutions termed particles. These particles are moved around the search space with a given velocity, yielding updated positions. Each particle's movement is influenced by promising locations found by other particles. The process is iterated until an optimal solution is obtained. In this paper, the PSO is used to optimize the stiffness values of a simplified structural model, in order to obtain a match between the model and the retrieved data. This is achieved by creating an initial set of particles locations $\mathbf{z}_1$, with random values assigned to each one of them, representing the values of mass and stiffness of the elements. This set is stored in a matrix of a dimension defined by the number of variables of the problem multiplied by the swarm size. A corresponding set of random initial velocities $\dot{\mathbf{z}}_1$ for the particles is also generated. The function is evaluated for each row of the swarm matrix, and the results are used to evaluate both the swarm's best position b^g and each single particle's best location b. The global position is taken as the row that provides the lower value for the optimization function. The local minima starts equal to the initial values assigned to each particle. When successive steps are evaluated, the local minima will be updated to the step value that minimizes the optimization function for that particle. For each particle, a new velocity is calculated using a unitary time step and the gained knowledge on the best location through the following expression:

$$\dot{z}_{h+1}^r = w\,\dot{z}_h^r + e_1\delta_1\left(b^r - z_h^r\right) + e_2\delta_2\left(b_h^g - z_h^r\right) \tag{2-28}$$

where δ_1 and δ_2 are random numbers between 0 and 1, b_r is the best location found for the r^{th} particle, b_h^g is the best global location at step h, w is the inertia of the particles, and e_1, e_2 are trust parameters. The inertia regulates the action of the swarm, with larger and smaller values yielding a global and local behavior, respectively. The trust parameters represent the confidence of a particle in itself, e_1, and in the whole swarm, e_2. The position of each particle is updated using their previous location and the previously calculated new velocity:

$$z_{h+1}^r = z_h^r + \dot{z}_{h+1}^r \Delta t \tag{2-29}$$

where z_{h+1}^r is the new location of the r^{th} particle, and Δt is a unitary value.

This updating scheme is repeated until difference in the optimization function between two consecutive steps at the best location is less than a predefined tolerance.

CHAPTER 3: INSTRUMENTATION PLAN

3.1 Accelerometers

The damage detection and estimation procedure is based on the idea of using the measured response of the system, at a limited number of DOFs (degrees of freedom), under normal levels of excitation, also defined as ambient vibrations conditions. In particular, in this study, vertical accelerations were measured in a limited number of positions along the structural elements of the tested systems.

The accelerometers used for this purpose are of two different types:

- Eight Seismic ICP® uniaxial piezoelectric accelerometers model 393C, from PCB (Figure 3.1), already preowned by the Iowa State Structural Engineering Research Laboratory. The characteristics for these sensors are listed in Table 3.1.

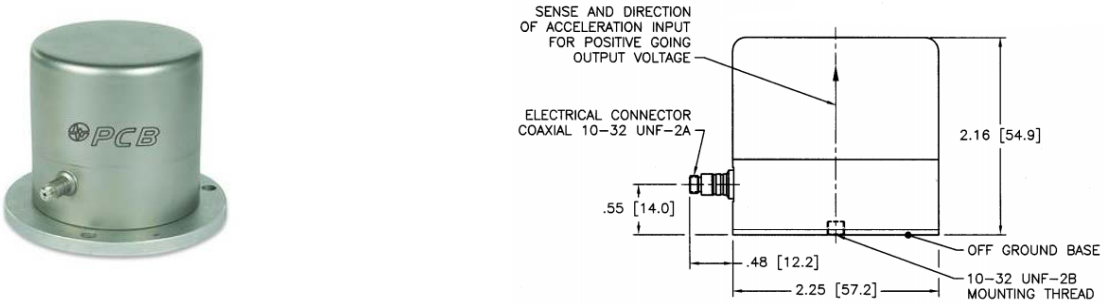

Figure 3.1: Seismic ICP® uniaxial piezoelectric accelerometers model 393C

- Four Seismic ICP® uniaxial piezoelectric accelerometers model 393B04, from PCB (Figure 3.2), purchased from PCB electronics for these tests. The characteristics for these sensors are listed in Table 3.2.

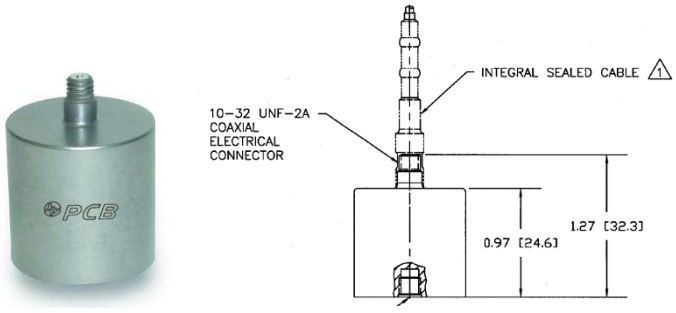

Figure 3.2: Seismic ICP® uniaxial piezoelectric accelerometers model 393B04

Table 3.1: 393C piezoelectric accelerometer specifics

Performance	
Sensitivity (±15 %)	1000 mV/g
Measurement Range	±2.5 g pk
Frequency Range (±5 %)	0.025 to 800 Hz
Frequency Range (±10 %)	0.01 to 1200 Hz
Resonant Frequency	≥3500 Hz
Broadband Resolution (1 to 10000 Hz)	0.0001 g rms
Non-Linearity	≤1 %
Transverse Sensitivity	≤5 %
Environmental	
Overload Limit (Shock)	±100 g pk
Temperature Range	-65 to +200 °F
Temperature Response	<0.03 %/°F
Base Strain Sensitivity	0.001 g/με

Table 3.2: 393B04 piezoelectric accelerometer specifics

Performance	
Sensitivity (±10 %)	1000 mV/g
Measurement Range	±5 g pk
Frequency Range (±5 %)	0.06 to 450 Hz
Frequency Range (±10 %)	0.05 to 750 Hz
Resonant Frequency	≥2500 Hz
Broadband Resolution (1 to 10000 Hz)	0.000003 g rms
Non-Linearity	≤1 %
Transverse Sensitivity	≤5 %
Environmental	
Overload Limit (Shock)	±300 g pk
Temperature Range	0 to +176 °F
Temperature Response	<0.03 %/°F
Base Strain Sensitivity	≤0.0005 g/με

All sensors used in the test were connected to the data acquisition system (DAQ) through general purpose coaxial cable model 002C from PCB electronics.

3.2 Position transducer

To corroborate the model obtained with the proposed damage detection method, the displacement of the two systems were monitored using a limited set of displacements along the centerline of the girders, to analyze the deflection shape under load and the residual deformations after each loading

phase. To collect these information, precise potentiometers were connected to the bottom faces of the girders. In this study, UniMeasure HX-PA series potentiometer were used. For each measured location, the instrument range was selected using the maximum expected deflection evaluated before the experiment. The characteristics for these sensors are listed in Table 3.3.

Table 3.3: Characteristics of Unimeasure HX-PA

Performance	
Linearity - From 2" to 6" - From 10" to 25" - All other ranges	 ±0.25 % Full Scale ±0.15 % Full Scale ±0.10 % Full Scale
Repeatability	±0.015 % Full Scale
Resolution	Essentially Infinite
Environmental	
Operating temperature	-40 to 203 °F
Storage Temperature	-67 to 212 °F
Operating humidity	100 %
Vibration	15 g's for max 0.1 ms.
Shock	50 g's for max 0.1 ms.

3.3 Servo-hydraulic actuator

To perform the test over the two specimens, a remotely controllable servo-hydraulic actuator was used in order to apply ambient vibration excitations to the systems. The particular actuator chose for this task is the RMK-220 Servo-Hydraulic inertial vibrator system (see Figures 3.3 and 3.4), which is a dynamic shaker with a good range of possible accelerations and corresponding forces (see Table 3.3). This range is achieved through the possibility of varying the number of additional masses mounted on the shaker; this number vary from none (corresponding to the first column of Table 3.3) to a maximum of 14 plates for an additional weight of 672 lb. (304.81 kg, third column of Table 3.3).

The shaker can be programmed, via LabVIEW, to apply different type of excitation signal. Since the actuator could work only in the displacement control mode, to have a measurement of the applied load an accelerometer (model 393B04) was mounted on the actuator, into a specific mount situated in the position shown in Fig. 3.3.

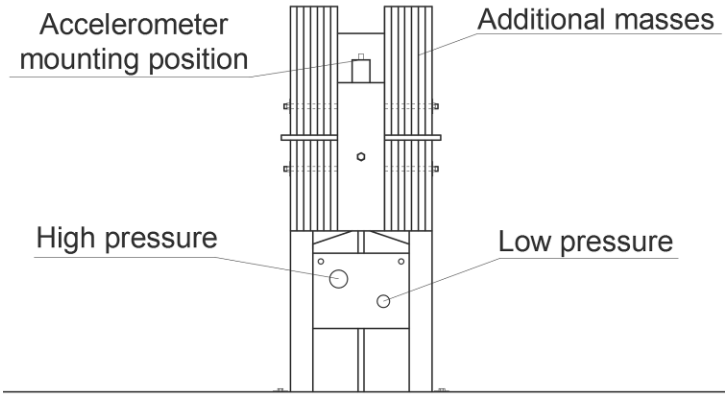

Figure 3.3: RMK-220 Servo-Hydraulic inertial vibrator design scheme

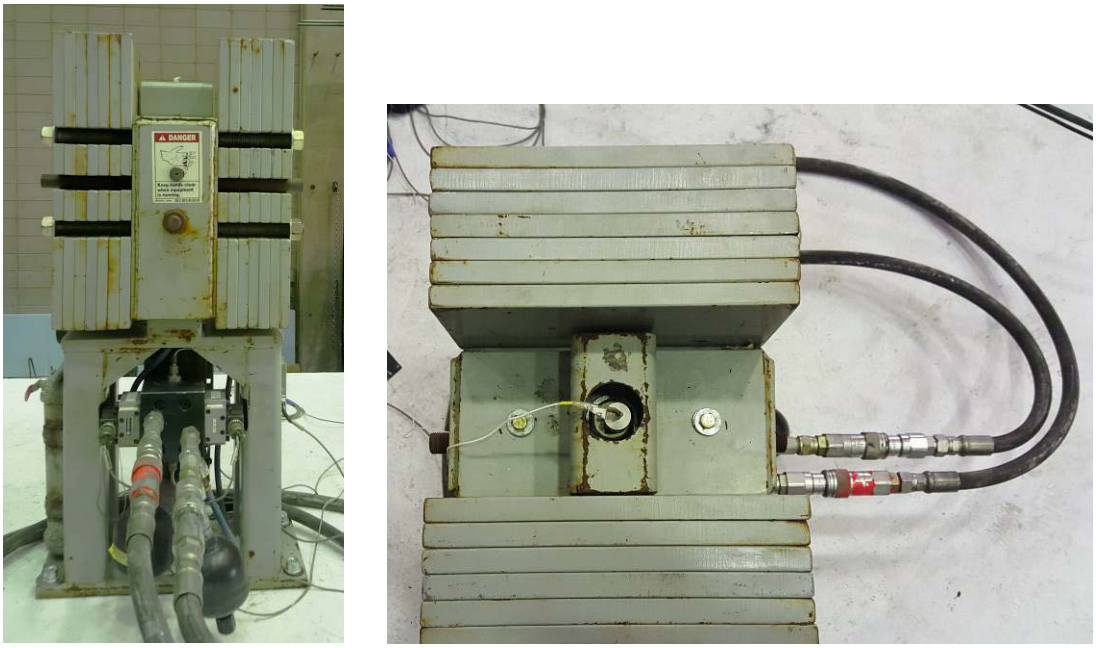

(a) (b)

Figure 3.4: RMK-220 actuator: (a) Frontal view; (b) Top view

Table 3.3: Frequency response of the RMK-220 shaker

Freq (Hz.)	Displacement (inches)	Velocity (ips)	Acceleration (g)	Force with carriage only(115 lbs mass) (lbf)	Force with6 of 14 plates (403 lbs mass) (lbf)	Force with 14 of 14 plates (787 lbs mass) (lbf)
1	+/- 0.5	6.	0.10	12.	41.	79.
2	+/- 0.5	12.	0.4	48.	164.	316.
4	+/- 0.5	24.	1.6	184.	656.	1,264.
8	+/- 0.5	48.	6.4	736.	2,000.	2,000.
16	+/- 0.25	48.	12.8	1,472.	2,000	2,000.
32	+/- 0.06	24.	12.8	1,472.	2,000	2,000.
64	+/- 0.016	12.	12.8	1,472.	2,000	2,000.
128	+/- 0.004	6.	12.8	1,472.	2,000	2,000.
256	+/- 0.001	3.	12.8	1,472.	2,000	2,000.

3.4 Data acquisition system

The data from the accelerometers were collected using three National Instruments NI9234 modules (four channels for each module, see Figure 3.5a). The chosen sample rate was 1652 Hz, which is the slowest sample rate offered by the NI9234 module.

The shaker was controlled using a National Instruments NI9263 module (Figure 3.5b) connected to the actuator control device (Figure 3.6). The generated time history applied using the hydraulic actuator was sampled at 1000 Hz, for all the various type of applied excitations (which are reported in Chapter 3)

(a) (b)

Figure 3.5: NI modules: (a) NI9234; (b) NI9263

Figure 3.6: RMK2200 controller box

All the modules were mounted on a National instrument Compact DAQ USB chassis (Figure 3.7), which was connected to a PC for the control of both signal generation and data acquisition.

Figure 3.7: NI Compact DAQ USB chassis

CHAPTER 4: DAMAGE DETECTION ALGORITHM

The proposed damage detection, location, and quantification method is divided into two sequential stages. First, acceleration data is analyzed using the SSID technique to extract the natural frequencies and mode shapes of the monitored system. This information is used to calculate the reduced order stiffness matrices of the system, after normalizing the mode shapes with respect to their 2-norm. Second, the modal properties and reduced order stiffness matrices are compared with the properties of the physical model. This comparison is conducted through three optimization functions, which are solved using the proposed PSO. Results of this optimization process are used to detect, localize, and quantify damage.

4.1 Stage I – Extraction of modal properties

In Stage I, the system's frequencies, $\boldsymbol{f}_{\text{retr}}$, and mode shapes, $\boldsymbol{\Phi}_{\text{retr}}$, are extracted using the SSID technique. This is achieved through the three-step method proposed by Ubertini et al. [20] discussed in at the end of the SSID section. Figure 4.1 shows typical raw data obtained from an SSID analysis using laboratory data from this work (to be described later), while Figure 4.2 shows the same data after filtering out the noisy modes. One can observe that after filtering, the first frequency of the system became immediately identifiable as the only stable frequency in the 0-10 Hz range. Clustering was used to identify the higher modes. The technique consists of aggregating the remaining modes into clusters that meet predefined criteria. The structural modes can be selected by analyzing the mode shapes of the clustered sets. Figure 3 shows an example of the clustering process results for the stable modes of the system (Figure 4.3), showing the 90% confidence interval for the damping (vertical lines) and the frequencies (horizontal lines). The first three identified modes of the system are encircled in the figure, where one intermediary mode (around 38 Hz) was not considered because it was associated with high damping. The retrieved mode shapes are normalized with respect to their 2-norm $\|\bullet\|$:

$$\boldsymbol{\Phi}_{\text{retr,i}} = \frac{\boldsymbol{\Phi}_{\text{retr,i}}}{\left\|\boldsymbol{\Phi}_{\text{retr,i}}\right\|} \tag{3-1}$$

where $\boldsymbol{\Phi}_{\text{retr,i}}$ is the i^{th} mode shape. The retrieved frequencies and normalized mode shapes are used to calculate the data-driven reduced order stiffness matrix $\bar{\boldsymbol{\kappa}}_{\text{red,S,data}}$ (Eq. (2-27)).

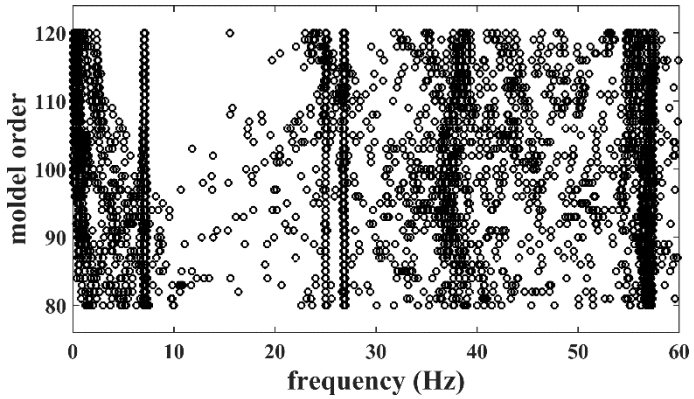

Figure 4.1: Retrieved frequencies versus model order n identified by the SSID algorithm before the elimination of noisy modes.

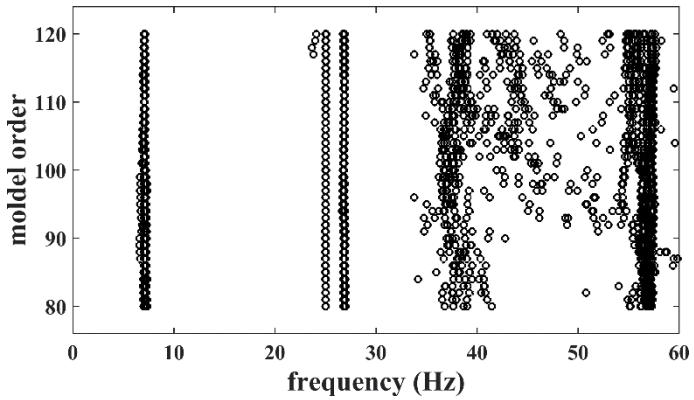

Figure 4.2: Retrieved frequencies versus model order n identified by the SSID algorithm after the elimination of noisy modes.

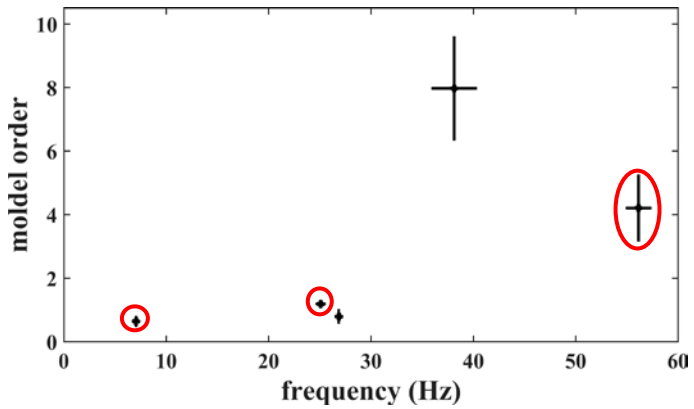

Figure 4.3: Retrieved frequencies versus damping ratios after the clustering process, showing the identified system modes encircled in red.

The procedure to conduct Stage I is presented in Algorithm 1:

4.2 Stage II – Damage detection and location

In Stage II, a finite element model of the structure is constructed, containing parameters that can be altered as a function of damage indices, α_i. These indices multiply the bending stiffness EI of the model's elements, where E is the Young's modulus of the material and I is the sections' moment of inertia, EI can differ between elements. Parameters α_i are selected based on an optimization function, which yield to an updated finite element model from which the model-driven dynamic parameters and reduced order matrices can be obtained. The described process is based on the assumption that the mass matrix of the system is known. However, if this assumption can be relaxed by accounting for mass variability by introducing a second set of coefficients β_i. This set will multiply the linear mass ρA_g of each model's element, where A_g is the cross-section area of the element and ρ is the material density. The remaining part of the process follows the same steps as the case of known mass, and therefore the rest of the section will focus on this case. Three different optimization functions are used to select parameters α_i, each solved independently, producing three different sets of damage indices. These optimization functions, termed OF_1 to OF_3, are defined as follows.

- Optimization function OF_1: the mean absolute percentage error between the retrieved frequencies and the frequencies obtained from the model.

$$OF_1 = \frac{1}{n_d}\sum_{d=1}^{n_d}\left(\frac{\left(f_{\text{retr},d} - f_{\text{func},d}\right)}{f_{\text{retr},d}}100\right) \tag{4-2}$$

where n_d is the number of selected frequencies, $f_{\text{retr},d}$ is the d^{th} retrieved frequency, and $f_{\text{funct},d}$ is the d^{th} frequency obtained from the model.

- Index J_2: the mean value of the standard deviation for the ratio of the computed and retrieved mode shapes.

$$OF_2 = \frac{1}{n_d}\sum_{d=1}^{n_d}\left(\frac{1}{(n_s - 1)}\sum_{s=1}^{n_s}\left(\Phi_{ds,\text{rt}} - \bar{\Phi}_{d,\text{rt}}\right)^2\right) \tag{4-3}$$

$$\Phi_{ds,\text{rt}} = \frac{\Phi_{\text{funct},ds}}{\Phi_{\text{retr},ds}} \tag{4-4}$$

$$\bar{\Phi}_{d,\text{rt}} = \frac{1}{n_s}\sum_{s=1}^{n_s}\left(\frac{\Phi_{\text{funct},ds}}{\Phi_{\text{retr},ds}}\right) \tag{4-5}$$

where n_s is the number of sensors, $\Phi_{\text{funct},ds}$ is the s^{th} component of the d^{th} mode shape function and $\Phi_{\text{retr},ds}$ is the s^{th} component of the d^{th} retrieved mode shape.

- Index J_3: the mean of the absolute value of all the terms in the SEREP error matrix. This matrix is defined as the absolute percentage error between the elements of the retrieved and the model's SEREP reduced order stiffness matrices

$$OF_3 = \frac{1}{n_s}\sum_{s=1}^{n_s}\left(\frac{1}{n_s}\sum_{z=1}^{n_s}\left(K_{S,\text{diff},sz}\right)\right) \tag{4-6}$$

$$K_{S,\text{diff},sz} = \left|\frac{\bar{K}_{\text{red},S,\text{data},sz} - \bar{K}_{\text{red},S,\text{funct},sz}}{\bar{K}_{\text{red},S,\text{data},sz}}100\right| \tag{4-7}$$

where $\bar{K}_{\text{red},S,\text{data},sz}$ and $\bar{K}_{\text{red},S,\text{funct},sz}$ are the elements in position sz of the retrieved and model's SEREP matrices, respectively.

These functions are solved using the PSO algorithm. Damage detection, location, and quantification is conducted by comparing all three sets of α_i selected by the particle optimization swarm. To detect damage, all of the three α_i for a given element need to be below unity, where unity is associated with undamaged condition. If all α_i are different than unity for a given element,

then damage is considered to be associated with that element, identifying the damage location. This criteria was established to minimize the identification of false positives. The quantification of damage corresponds to the average value of α_i for that particular element. For example, an average value of α_i= 0.6 would signify an element at 60% of its original health, or 40% damaged. Algorithm 2 details the implementation procedure of the damage detection approach.

Algorithm 2 Damage detection algorithm - Stage II

$\text{Clustered}_{\text{data}} \leftarrow$ Import from Stage I
$OF_1 \leftarrow Eq.(31)$
$OF_2 \leftarrow Eq.(32)$
$OF_3 \leftarrow Eq.(35)$
$Swarmsize, N_{variables}$ ▷ Number of particles and problem variables
$toll \leftarrow 10^{-4}$ ▷ Stopping criteria value
Initializing damage indices
for $j \leftarrow 1, 3$ **do**
    $\alpha_{i,OF_j} \leftarrow \Re^{Swarmsize \times N_{variables}}$
end for
Parallel evaluation of the functions
for $j \leftarrow 1, 3$ **do**
    $OF_{j,1} = OF_j\left(\alpha_{i,OF_j}\right)$
    $k \leftarrow 2$
    while $OF_{j,k} - OF_{j,k-1} \geq toll$ **do**
        $b_k^g \leftarrow \min\left(OF_{j,k}\right)$
        $b^r \leftarrow \min\left(OF_{j,k}\left(r\right), OF_{j,k-1}\left(r\right)\right)$ ▷ $r = 1 \div Swarmsize$
        $k = k + 1$
Parallel evaluation of the functions optimization
        for $r \leftarrow 1, Swarmsize$ **do**
            $\dot{z}_(k+1)^r \leftarrow Eq.(28)$
            $z_(k+1)^r \leftarrow Eq.(29)$
        end for
    end while
    $\alpha_{OF_j} \leftarrow \min\left(OF_{j,k}\left(r\right)\right)$
end for
for $r \leftarrow 1, N_{variables}$ **do**
    if $\alpha_{OF_1}\left(r\right)$ & $\alpha_{OF_2}\left(r\right)$ & $\alpha_{OF_3}\left(r\right) < 1$ **then**
        $\alpha\left(r\right) \leftarrow \text{mean}\left(\alpha_{OF_1}\left(r\right), \alpha_{OF_2}\left(r\right), \alpha_{OF_3}\left(r\right)\right)$
    else
        $\alpha\left(r\right) \leftarrow 1$
    end if
end for

CHAPTER 5: VALIDATION OF SIMULATION RESULTS

The first step in establishing a reliable and robust damage detection algorithm consists in its validation using simulated data, which will represent realistic damage scenarios that the algorithm will have to address. In this study, two different system of increasing complexity were simulated. The first simulation involved the use of a single simply supported reinforce concrete (RC) beam. For this case different damage scenarios were analyzed, to study the reliability in the identification and quantification of localized and scattered damage. The second simulated system was selected to study the performance of the algorithm in a more complex scenario. This system is defined by two RC girders, with applied un-bounded post-tension, connected using a RC deck. In this case a differential damage scenario was simulated, to asses if the algorithm was capable of correctly quantify damage in a single structural element. The following subsections will present in detail the detail of the simulated system as well as the obtained results.

5.1 Single RC girder

The simulated system consists of a simply supported reinforced concrete beam of 13.0 m (42.65 ft.) length. The beam, illustrated in Figure 5-1, is discretized into 16 elements of equal length and a rectangular cross-section of 0.3×0.6 m^2 (11.8×23.6 in^2). Two different damage scenarios are simulated to assess the robustness and the versatility of the proposed approach. In the first scenario, damage is introduced in the system by reducing the moment of inertia for elements 7 and 8 by 20 and 30 %, respectively, to represent the effects of crack formation. The second scenario represent the formation of damage in two different locations, by reducing the moment of inertia for elements 9 and 13 by 30 and 20 %, respectively. The beam is excited using a dynamic moving load that mimics the passage of a vehicle (shown by F(t), Figure 5.1) for a total duration of 60 s. This type of excitation was selected to test the robustness of the algorithm over non-ideal conditions. When the excitation is not white noise, its frequency will appear in the retrieved modal properties. However, using the method proposed by Ubertini et al. [20], it is possible to overcome this problem by automatically eliminating this spurious pole. Such result is quite relevant to field applications, where the excitation cannot always be characterized as white noise. Gaussian white noise was added to the excitation force to simulate the ambient vibrations. This noise was characterized using the signal-to-noise (SNR) ratio, expressed in dB:

$$SNR = 20\log_{10}\left(\frac{A_{signal}}{A_{noise}}\right) \tag{5-1}$$

where A_{signal} is the root mean square of the noisy signal (i.e., the excitation force), and A_{noise} is the root mean square of the noise. For this study, the SNR was set to 70 dB. The application of white noise in the excitation force generated an SNR of 11.25 dB or 37.7% noise in the collected response data. The apparent high amplification of the noise level from the excitation to the response is due to the fact that both the exciting force and the white noise generate a comparable level of acceleration in the system. Figure 5.2 plots the acceleration response from the force (i.e., noise-free) and from the noise itself. These responses have comparable magnitude generating a high level of SNR in the final response. In this study, a low magnitude force was selected in order to produce a high level of noise for assessing the robustness of the SSID identification process.

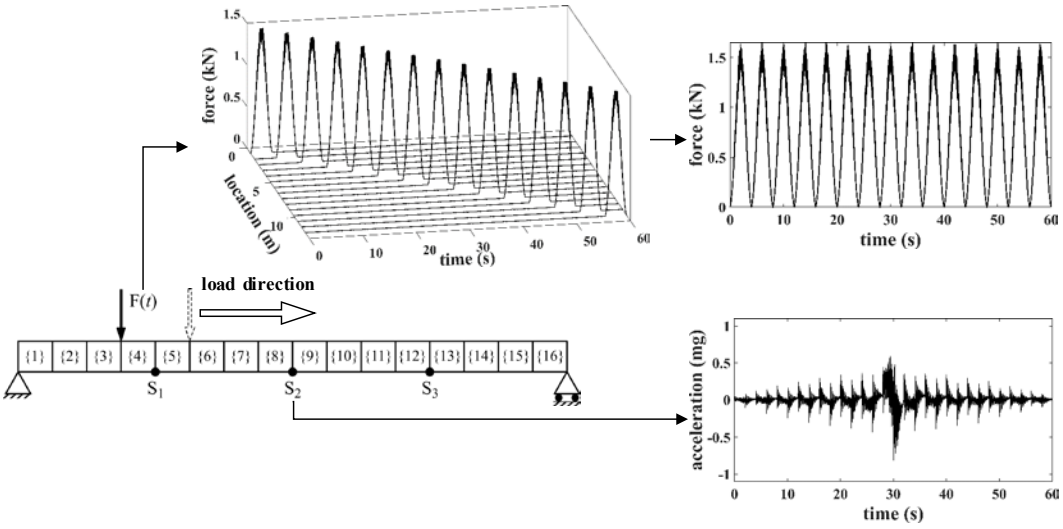

Figure 5.1: Simulated simply supported RC girder showing element discretization, sensors locations (s_1, s_2, and s_3), and example of force input and acceleration response time series

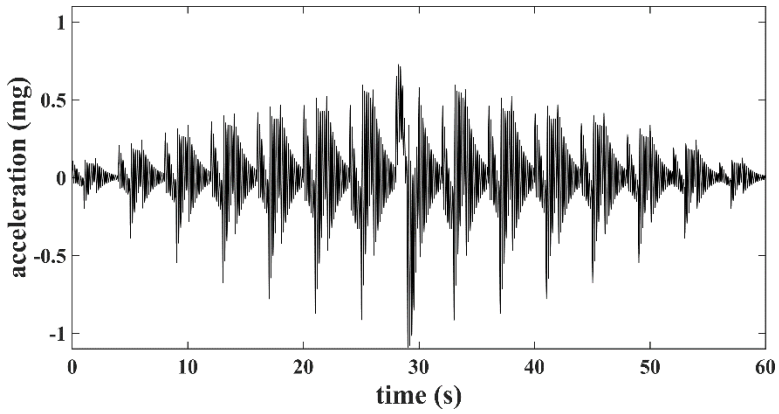

(a)

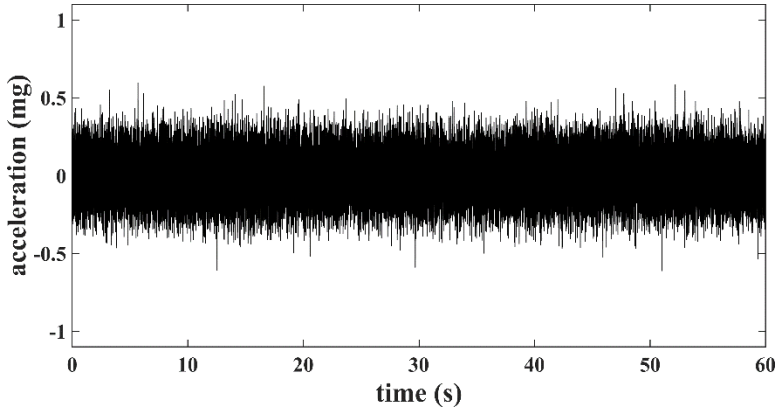

(b)

Figure 5.2: Responses of the system from the noise-free (a) and noise-only (b) simulations.

Rayleigh damping was used in the simulation, assigning to the first two modes a damping ratio of 3%. The corresponding structural response was taken at three locations of simulated three sensors (locations S_1, S_2, and S_3 in Figure 5-1). Figure 5-2 shows plots of a typical excitation and a corresponding numerically measured acceleration time series.

Results from the modal properties extraction process using SSID for the first three modes in the first scenario are listed in Table 5.1. There is excellent agreement between the modes from the model and those extracted using SSID.

Table 5.1: First three frequencies of the system, retrieved with SSID and calculated from the model

	model frequency (Hz)	SSID frequency (Hz)	error (%)
1	5.510	5.514	0.07
2	22.786	22.759	-0.12
3	50.176	50.202	0.05

For each scenario, the modal properties retrieved after damage are used to construct the three optimization functions (OFi) along with a surrogate beam model. In each PSO analysis, the values of the damage indices α_i were allowed to vary between 0.4 and 1.0. The PSO for these functions yielded three sets of damage indices for each scenario, α_i, listed in Table 5.2. For the first scenario, results showed that only elements 7 and 8 passed the rejection criteria, since all their damage indices, $\alpha_{i,}$, were smaller than unity for all three optimization functions. The average α_i values for elements 7 and 8 were $\alpha_7 = 0.81$ and $\alpha_8 = 0.73$, respectively, which correspond to identified damages of 19% and 27% comparable with the simulated damages of 20% and 30%, for element 7 and 8, respectively. Similarly, in the second damage scenario, results identify damage only at elements 9 and 13. The average damage indices returned a value of $\alpha_9 = 0.72$ and $\alpha_{13} = 0.79$ for elements 9 and 13, respectively, yielding and identified damage intensity of 28% and 21% that compares well with the simulated damage of 30% and 20%, respectively. Under both damage cases, the algorithm correctly identified the damage location and its intensity. However, the PSO algorithm includes random generations (Eq. 2-28) that could affect the results. To evaluate the effect of such randomness, the second damage scenario was analyzed using five different runs. In each run, the random number generator used in the Matlab environment was changed in type and seed. The results of this analysis, in terms of the final average indices, are shown in Figure 5.3. All of the five runs detected and diagnosed damage under elements 9 and 13 only. The average value of the damage indices between all the runs was equal to $\alpha_9 = 0.72$ and $\alpha_{i3} = 0.80$ for elements 9 and 13, with a standard deviation of $\alpha_{\sigma 9} = 0.02$ and $\alpha_{\sigma 13} = 0.01$, respectively. These results indicate that the PSO's random generation feature has limited effect on the localization and identification of the damage intensity.

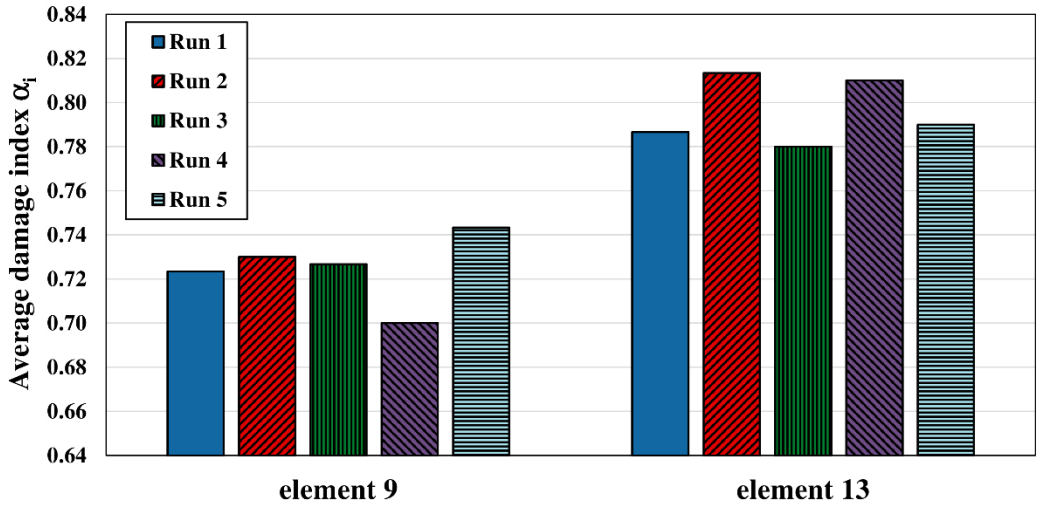

Figure 5.3: Variation of the average damage index α_i between different runs for elements 9 and 13

The retrieved modal properties are then used to construct the three optimization functions (OF_i) along with a surrogate beam model. The PSO for these functions yielded three sets of damage indices for each scenario, α_i, which are listed in Table 5.2. For the first scenario results showed that only elements 7 and 8 passed the rejection criteria, since all their damage indices α_i were smaller than unity for all three optimization functions. The average α_i values for elements 7 and 8 were $\alpha_7 = 0.81$ and $\alpha_8 = 0.73$, respectively, which correspond to an identified damage of 19% and 27%, compared with the simulated damages of 20% and 30%, for element 7 and 8, respectively. Similarly, in the second damage scenario results indicate presence of damage only in element 9 and 13, for which the rejection criteria was not met. The average damage indices assume a value of a9= 0.73 and a13=0.84 for elements 9 and 13 respectively, yielding and identified damage intensity of 27% and 17% that compares well with the simulated damage of 30% and 20%, respectively.

From these results is possible to conclude that in a simulated environment the proposed algorithm is accurate and adaptable to different damage situations. The accuracy of the results are higher when significant damage is concentrated in the mid-span of the beam. However, the algorithm results are accurate even in a staggered damage situation, with multiple location of damage located in non-adjacent elements.

Table 5.2: Damage indices α_i obtained from the particle swarm analysis for the three optimization functions.

element number	first damage scenario				second damage scenario			
	OF_1 α_i	OF_2 α_i	OF_3 α_i	final α_i	OF_1 α_i	OF_2 α_i	OF_3 α_i	final α_i
1	1.00	0.40	0.93	1.00	1.00	0.40	1.00	1.00
2	1.00	0.70	0.99	1.00	1.00	1.00	1.00	1.00
3	1.00	1.00	1.00	1.00	1.00	1.00	1.00	1.00
4	1.00	0.95	1.00	1.00	1.00	1.00	1.00	1.00
5	1.00	0.97	0.98	1.00	1.00	1.00	1.00	1.00
6	1.00	0.94	0.52	1.00	1.00	1.00	1.00	1.00
7	**0.81**	**0.95**	**0.68**	**0.81**	1.00	0.78	1.00	1.00
8	**0.70**	**0.67**	**0.81**	**0.73**	1.00	1.00	1.00	1.00
9	0.88	1.00	0.85	1.00	**0.73**	**0.75**	**0.72**	**0.72**
10	1.00	0.77	0.84	1.00	1.00	1.00	1.00	1.00
11	1.00	0.91	0.92	1.00	1.00	0.78	1.00	1.00
12	0.95	1.00	0.96	1.00	1.00	0.94	1.00	1.00
13	0.90	1.00	1.00	1.00	**0.68**	**0.88**	**0.79**	**0.79**
14	1.00	0.52	0.98	1.00	1.00	1.00	1.00	1.00
15	1.00	0.96	0.98	1.00	1.00	1.00	1.00	1.00
16	1.00	1.00	0.97	1.00	1.00	1.00	1.00	1.00

5.2 Double RC girder

The previous section showed the good performance of the algorithm in the identification and quantification of damage in a single structural element. However, bridges are structural systems built from a multitude of structural elements interconnected to generate the required capacity to sustain vehicular traffic. Therefore, the next step to test the performance of the damage detection algorithm was its application to simulated data from a more complex structural system. In this study, a system composed of two RC concrete girders connected by a RC deck was designed for both simulation and experimental validation. Figure 5.4 illustrates a scheme of the simulated system, were the dynamic load represents a moving impact load applied to the surface of the deck.

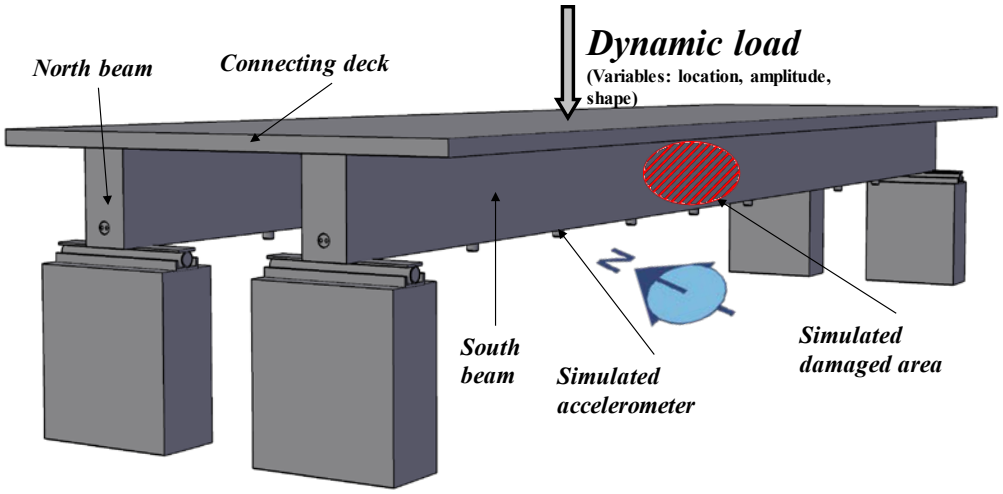

Figure 5.4: Scheme of the double beam simulated system

The system was designed to be representative of a short-span bridge, both statically and dynamically. Figure 5.5 illustrates the cross-sections dimensions for the whole system and for each single girder. The full system has a total width of 108 in. and a total depth of 23 ½ in. The girders have a rectangular cross section of 10×20 in and are placed at a distance of 54 in. Each girder is reinforced with a single unbounded 1in post-tension bar located at 7" in from its bottom. The use of the post-tension bar was necessary to avoid early cracking and to control the system deflection, as specified in section 6.??. The span of the two girders was set equal to 31.5 ft in order to obtain a first frequency which is in the typical range of short-span bridges (between 10-12 Hz).

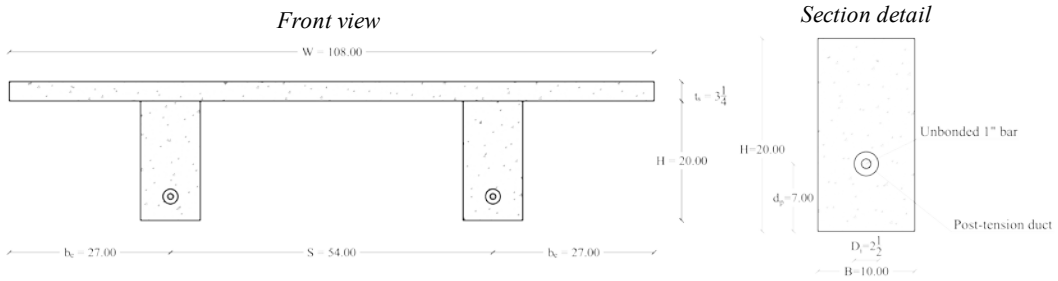

(a) (b)

Figure 5.5: Cross-section dimensions for (a) the system and (b) the single girder. (all dimensions are in inches)

Differently from the example shown in section 5.1, the simulation of the system was conducted in OpenSees platform that is an open source structural program. This program was chosen due to its flexibility in the definition of a structural system and the possibility of integration with Matlab for the damage detection process. To accurately simulate a system subjected to a variable dynamic load, such as a variable impact load on the surface of the deck, it is necessary to build a high-fidelity finite element (FE) model of the system. However, an excessive complexity of the model will lead to high simulation time and difficulty in integration with the damage detection algorithm. To maximize the accuracy of the model while keeping the model relatively simple, the team implemented a mixed solution that integrates beam and shell elements. Figure 5.6 shows the structural scheme defined in Opensees were the two girders are modeled using elastic beam elements of constant section, while the deck is defined by four nodes elastic shell elements of constant thickness. Both the beam and shell elements are defined on the barycenter of the respective elements, and are connected through beam rigid links constraints in correspondence of the beams elements nodes. Using beam element for the girders reduces the computational burden, in respect of shell or solid elements. Meanwhile, modelling the deck with shell elements help to correctly represent its contribution to the system and enhance the ability to locate the moving load in an ample array of locations over the surface of the deck.

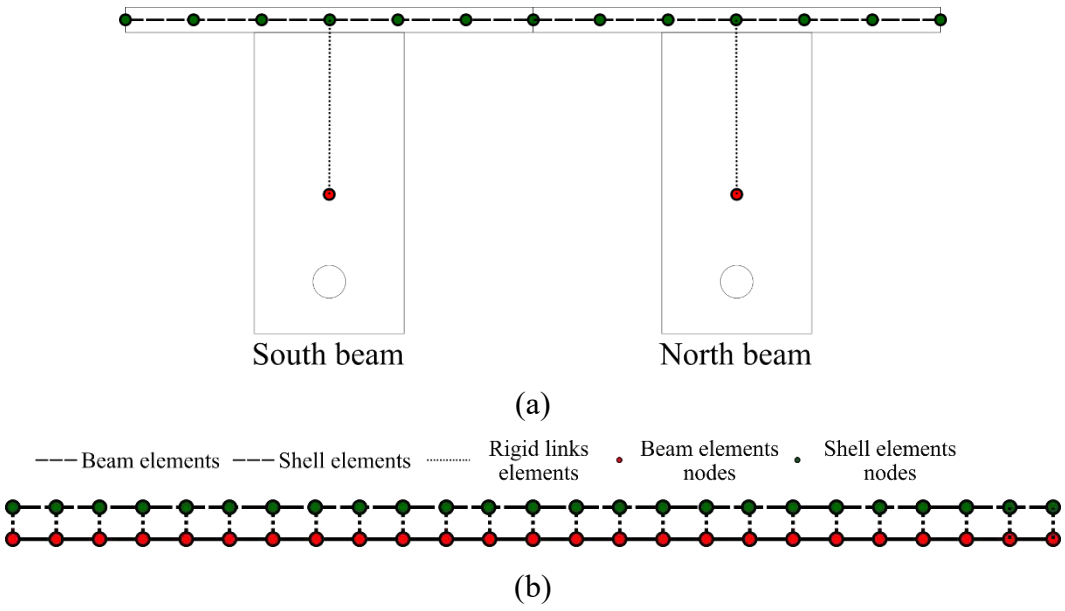

Figure 5.6: Opensees elements and connection scheme of the simulated system: (a) frontal view and (b) side view

In this study each girder was divided in 24 elements of equal dimension (15 ¾ in) and modelled using the Elastic Beam Column Element of the Opensees library (Figure 5.6). On the other hand, the deck was partitioned using a mesh of dimensions 9×15 ¾ in that was used to define the array of shell elements. Among the different choices for this type of elements in Opnesees, ShellMITC4 element combined with an Elastic membrane plate section was used to represent the constant thickness of the deck. The achieve a system behavior, these two types of elements were connected through a rigid link constraint. This multi-point (MP) constraint forces a slave node — in this case the deck— to follow the master node—the beam— in both rotational and translational degrees through a constraint matrix that depends on the relative location of the two nodes. It must be noted that to enforce a MP constraint in Opensees, specific numerical methods are used to build the system stiffness and mass matrix.

An additional advantage of this modelling approach resides in the interchangeability of the beam elements, which could be replaced with non-linear ones obtaining a model that accurately represent post-linear behavior of the system. In the first part of the study the model was kept in linear range so that the results would be comparable with the single beam case. This was achieved by introducing a differential damage as a reduction of the moment of inertia, *I*, of the north beam in the central elements. As shown in Figure 5.7, in the central portion of the north beam damage was introduced on four elements, with an intensity of 30% for two of them and 20% for the remaining two.

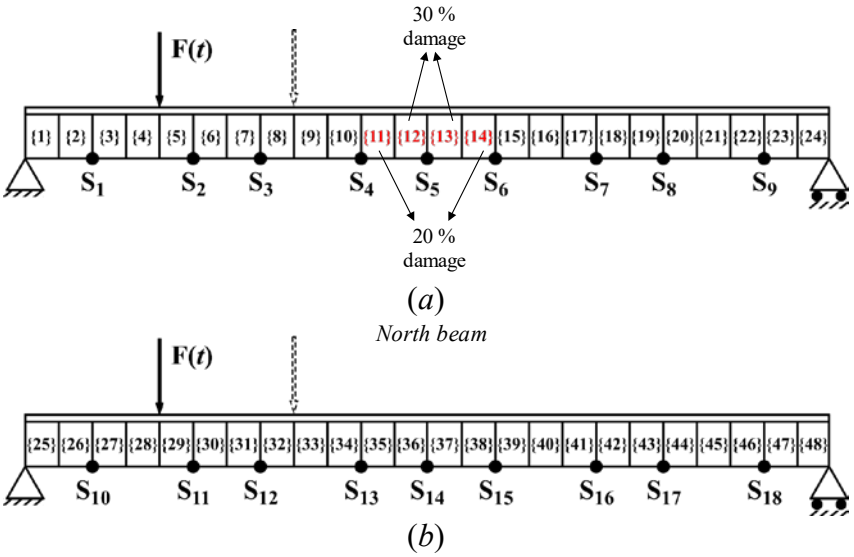

Figure 5.7: Element subdivision, sensors location and simulated damage intensity for the north (a) and the south (b) beams

The system was excited using a moving impact load, travelling along the centerline of both beams. The load is first applied to the north beam, moving in one direction, and then to the south beam while travelling in the opposite direction (Figure 5.8). The response of the system is collected at 18 locations equally distributed between the two girders, as shown in Figure 5.4, marked as S_1 to S_{18}.

To implement the damage detection algorithm in this simulation, the algorithm was modified by including the Opensees model in the process. More specifically, the bending stiffness multiplier α_i are applied to the beam elements in the Opensees model. The algorithm is initialized in Matlab with a set of random α_i, these are then transmitted to Opensees that evaluates the frequencies and mode shapes of the model with said multipliers. The results are sent to Matlab that evaluates the corresponding function (Equations 5-2 to 5-7) and evaluates the new set of indices. This process is repeated until the stopping criteria for the algorithm is met. Figure 5.8 presents a flow chart that exemplifies the exchange of information between the two software.

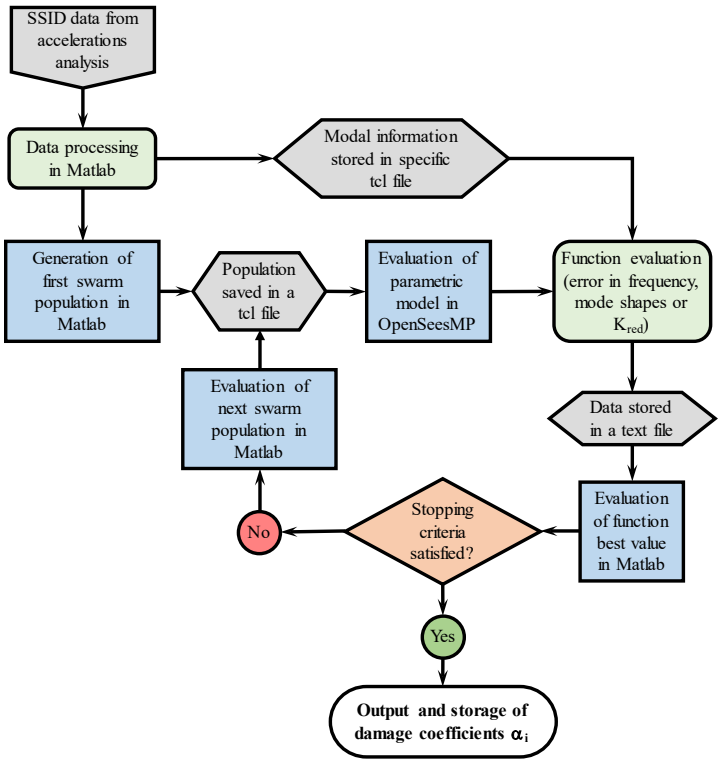

Figure 5.8: Flow chart of the Matlab-Opensees information exchange for the damage detection algorithm.

Figure 5.9 shows the average values of the damage indices α_i obtained with the modified damage detection algorithm. As it is possible to see the damage location is correctly identified with no false positives. The identified damage indices for the four elements are equal to 0.8, 0.71, 0.68 and 0.81 which translates in an identified level of damage equal to 20, 29, 32 and 19 %. These correlates very well with the simulated level of damage which are equal to 20, 30, 30 an 20 %, respectively.

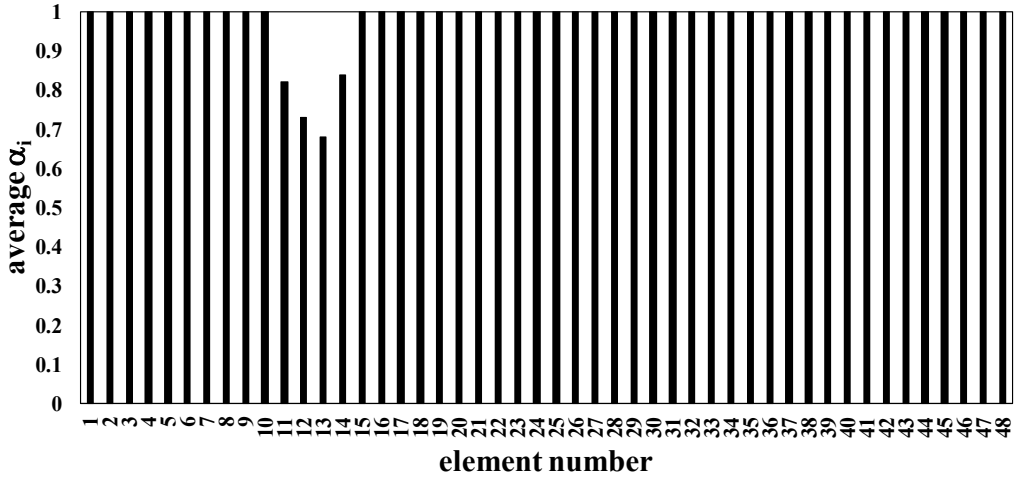

Figure 5.9: Average damage indices α_i retrieved with the modified damage detection algorithm

CHAPTER 6: EXPERIMENTAL PLAN

To validate the damage detection algorithm full-scale experiment were conducted. The experimental plan consisted of a full-scale girder with a partial deck casted on its central part. The beam was subjected to dynamic excitation in three different damage states, and the collected accelerations were used to evaluate the performance of the damage detection algorithm. The following test consisted of two RC girders, post-tensioned with a single unbounded bar and connected using a RC concrete deck, representing a portion of the bridge deck with two girders. In this case in one of the girders the post-tension was removed to guarantee the appearance of differential damage between the two sides. After this stage, the system was tested under a variety of damage scenario ranging from the appearance of incipient damage to the formation of a significant number of cracks along both girders. At each stage, dynamic data were collected under a series of impulsive excitations applied to the top surface of the connecting deck. The collected data were used to validate the damage detection process for the complex system. The following section will describe in detail all the analysis and results of these experiments.

6.1 Single PC girder – BTC60

The first laboratory experiment is conducted on a full-scale pretensioned girder built with a partial cast-in-place deck (Identified as BTC60 hereafter). It was a standard pre-stressed bulb-tee type C girder designed by the Iowa Department of Transportation with a span of 18.3 m (60 ft). BTC60 was part of a larger set of experiments conducted for the NCHRP project 12-94. The girder had a depth of 1.14 m (45 in) and its partial deck is extended symmetrically about the mid-span over a total length of 6.80 m (22.3 ft); flexural cracking on the girder was expected outside the mid 6.8 m of the girder. Figure 6.1 shows the cross-sectional dimensions of both the girder (Figure 6.1(a)) and composite (Figure 6.1(b)) sections. The girder was built using a 41.36 MPa (6 ksi) concrete with eight 1.52 mm (0.6 in.) low relaxation strands, applying a total initial prestressing force of 1514 kN (340.3 kips). The deck was cast in place using a specified concrete strength of 27.60 MPa (4 ksi). The concrete strengths on the day of testing were 51.17 MPa (7.42 ksi) and 33.15 MPa (4.81 ksi) for the girder and deck, respectively. Table 6.1 report a summary of the concrete strength of the different components for different maturation stages.

Table 6.1: Summary of concrete compressive strength for the specimen components at different maturation stages

Element	Age (days)	Compressive strength (MPa)	Compressive strength (ksi)
BTC60	2	35.30	5.12
	7	42.54	6.17
	34	48.47	7.03
	58	50.33	7.30
	62 (TD)	51.17	7.42
Deck	8 (TD)	33.15	4.81

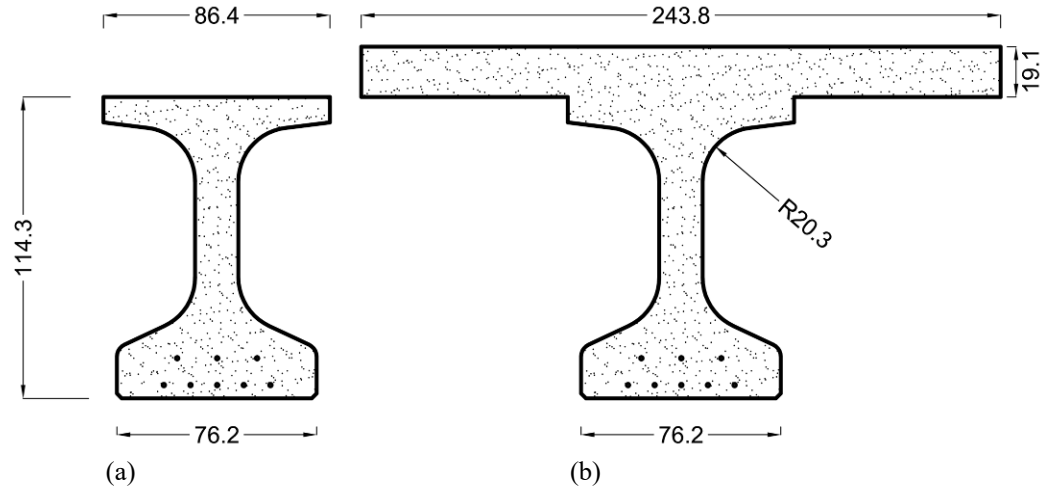

Figure 6.1: **BTC60: schematic of (a) girder; and (b) composite cross sections (all dimensions in centimeters).**

To acquire dynamic response measurements, BTC60 was excited using an RMK-2200 servo hydraulic shaker, controlled through the LabVIEW environment, applying a white noise excitation over 80 s with an amplitude of ± 4.45 kN (1 kip) and standard deviation of 0.89 kN (0.20 kip), which generated response accelerations ranging between 50-150 mg. The shaker was offset by 1.52 m to the side of the girder's center line, which corresponded with the possible installation position closest to the center line due to the presence of loading equipment. Four 16 mm bolts for concrete were used to secure the shaker to the girder. Figure 6.2 and Figure 6.3 show the shaker location in the experimental setup. For safety, chains were used to loosely connect the beam ends to the supports (Figure 6.2). The response of the structure was collected using nine accelerometers mounted to the bottom surface of the girder, and one accelerometer installed on the

actuator masses. Two different types of Seismic ICP uniaxial piezoelectric accelerometers were used for this experiment: five model 393C, and four model 393B04 from PCB. Data was acquired through LabVIEW environment using four NI9234 modules with a sampling rate of 1652 Hz. Figure 6.2 shows the location of the shaker and sensors whereas Figure 6.3 illustrates the experimental setup.

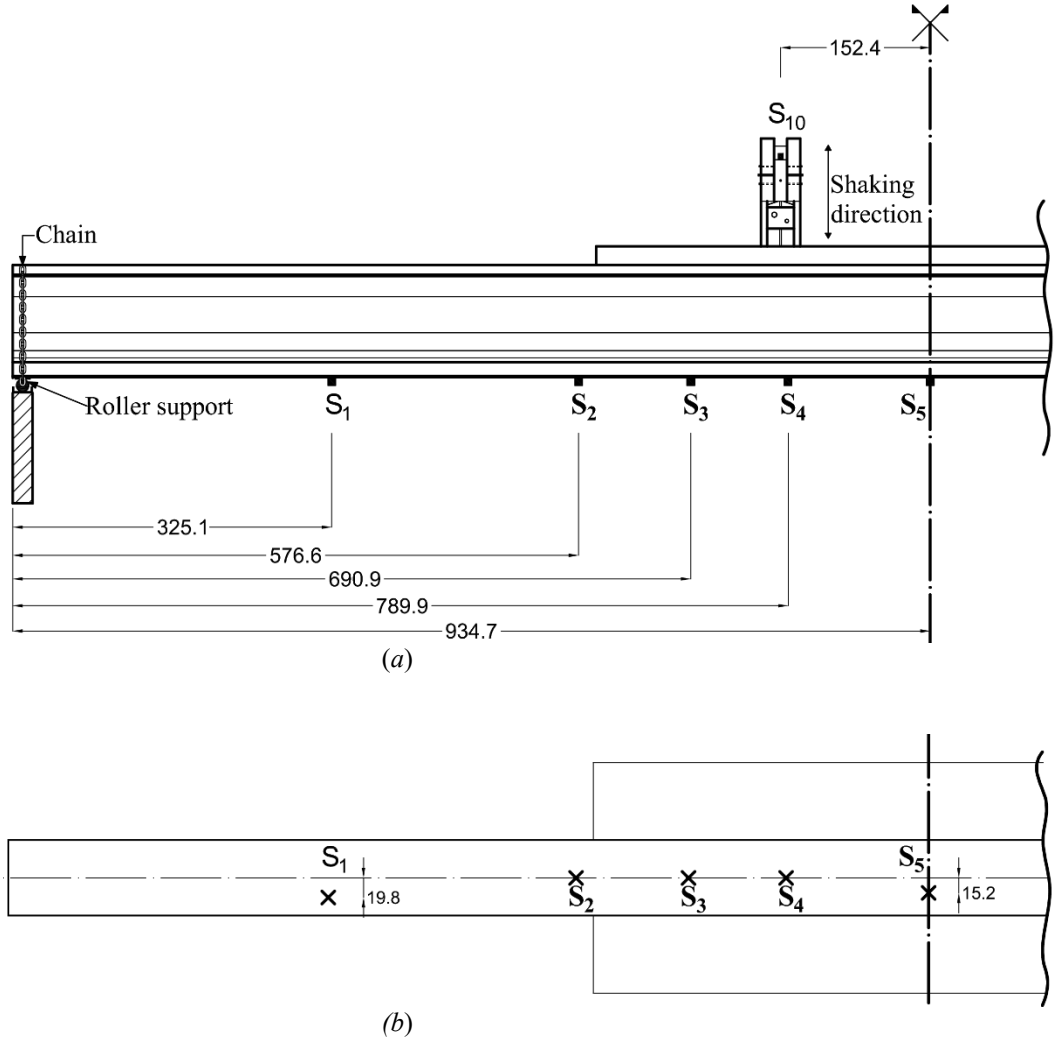

Figure 1.2: **Sensors and shaker locations (a) side view and (b) bottom view (all dimensions in centimeters, sensors S_6 to S_9 are placed symmetrically in respect to the mid-span).**

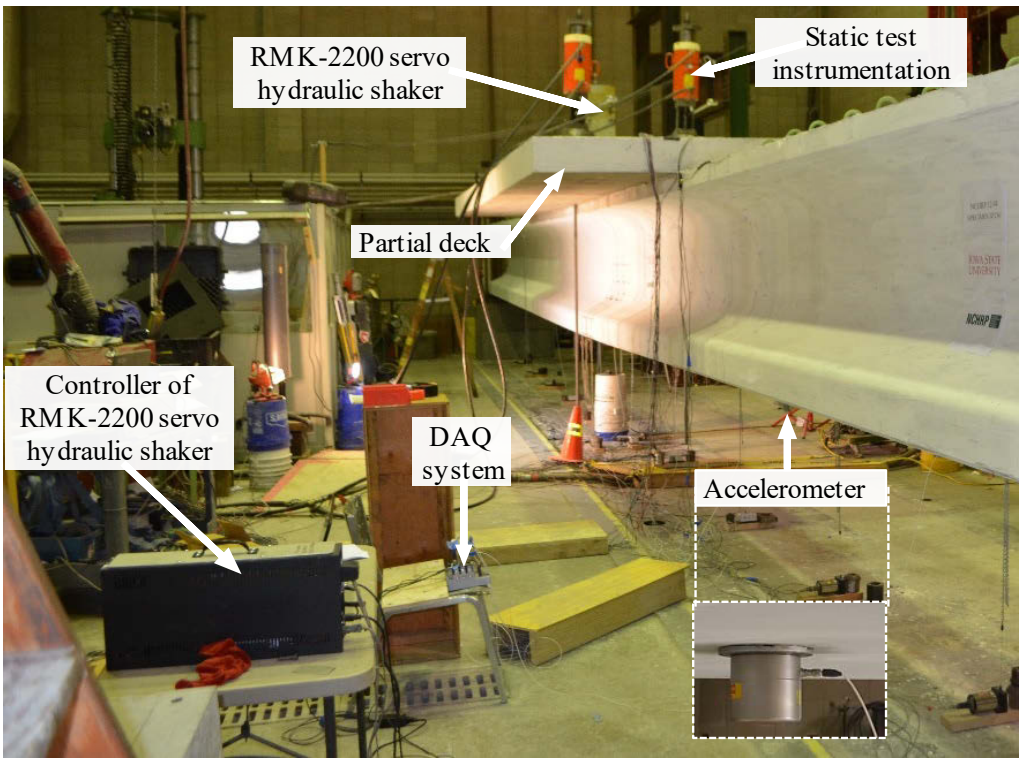

Figure 6.3: Experimental setup of BTC60 with seismic ICP® uniaxial piezoelectric accelerometers model and the hydraulic shaker.

Three different damage cases were considered. Damage was induced in the girder using a pair of actuators mounted onto the top of the beam (Figure 6-3). These damage stages are characterized by the intensity of the load applied to the girder, summarized as follows:

- No damage: The girder was subjected to a monotonic quasi static load with amplitude of 44.5 kN (10 kips). Upon reaching this value, the beam was fully unloaded and a dynamic shaking test was performed. This first loading step ensured that the system was behaving as expected in the undamaged elastic region. This first test was aimed at acquiring measurements for the undamaged condition of the structure, representing the stiffness of the undamaged specimen.
- Damage case 1: The next step in the loading protocol of the beam consisted of reaching 80% of the predicted yield load of the girder-deck system, corresponding to 355.9 kN (80

kips). Under this load the girder experienced a deflection of 2.54 cm (1 in). During this phase, the formation and growth of 10 to 13 flexural cracks, in the portion of the girder within the partial deck, was confirmed by visual inspection. Following the visual confirmation of damage, the beam was unloaded and subjected to the dynamic shaking test.

- Damage Case 2: The final damage stage represents the condition where the strands in the extreme location of the girder have reached the first yield limit state, which occurred at 452.4 kN (101.7 kips). A mid-span deflection of 8.1 cm (3.19 in) was recorded. Due to the high load both the extension of the previously formed cracks and the formation of new ones were

6.2 Double RC girders with full deck

The second part of the experimental campaign was conducted on a full-scale system representing a portion of a short span bridge. The system is composed of two reinforced concrete (RC) girders, slightly precompressed, and connected by a deck. The two girders have a rectangular cross section of 25.4 × 50.8 cm (10.0 × 20.0 in.). The beam dimensions were decided such that the first natural frequency of the full system would be limited to below 12 Hz, therefore to avoid early cracking under their self-weight they were both subjected to post-tension. To accommodate a single post-tension bar of 2.54 cm (1 in.) diameter, a circular plastic duct of 6.35 cm (2.5 in.) was included in the cross section with its center located at 17.78 cm (7.0 in.) from the bottom face of the girder. To guarantee high ductility of the girders, needed to achieve the highest damage cases, the sections were reinforced using 6 #8 rebars, which have a diameter of 25.4 mm (1.0 in.), positioned as indicated in Figure 6.4.

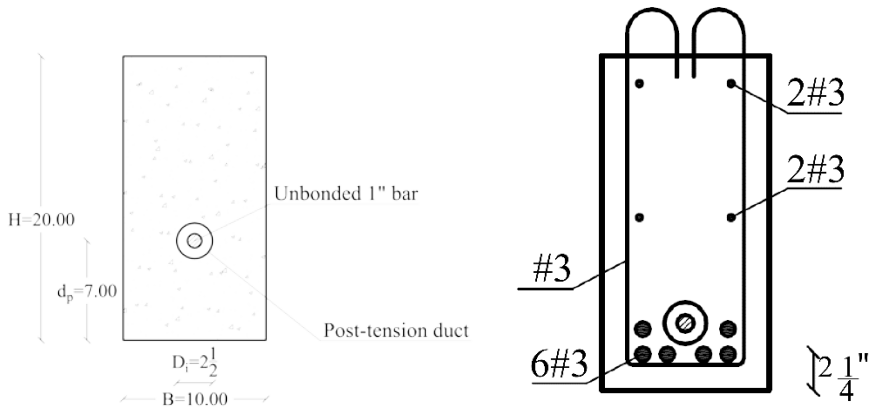

Figure 6.4: Cross-section dimensions (a) and rebars locations (b) for the girder section (all

dimensions are in inches)

The girders were casted in the Iowa state university structures laboratory (Figure 6.5) using a 41.36 MPa (6 ksi) self-compacting concrete (SSC). Upon reaching 14 day of maturation both beams were post-tensioned, while on the ground, with a total force of 391.44 kN (88 kips) applied through a hydraulic jack to the 1" Williams post-tension bars.

(*a*) (*b*)

Figure 6.5: RC girder before (a) and after (b) the concrete pour

Afterwards, the girders were moved to their final location over the supports (Figure 6.6) using the structural laboratory 20 ton crane. The total length of the two girder is 10.06 m (33 ft.), while the distance between the two supports is equal to 9.60 m (31.5 ft.)

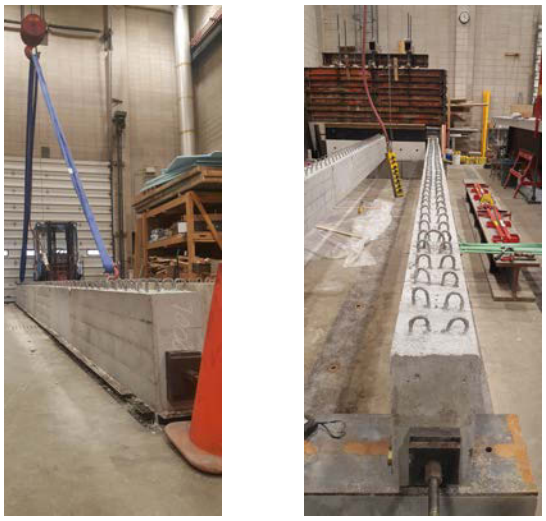

Figure 6.6: RC girder before (a) and after (b) their movement over the supports.

Once the beams were placed in their final location, the construction of the cast-in-place deck was started. The deck connecting the two girders had a width of 2.74 m (9 ft.) and a thickness of 8.89 cm (3.5 in.), while its total length is equal to the length of the girders. The deck was designed to insure the formations of cracks only on the girders for all the analyzed damage scenarios, except the final collapse of the structure. Therefore, the deck was reinforced using two layers of #4 rebar, on both the bottom and the top surface as shown in Figures 6.7 and 6.8.

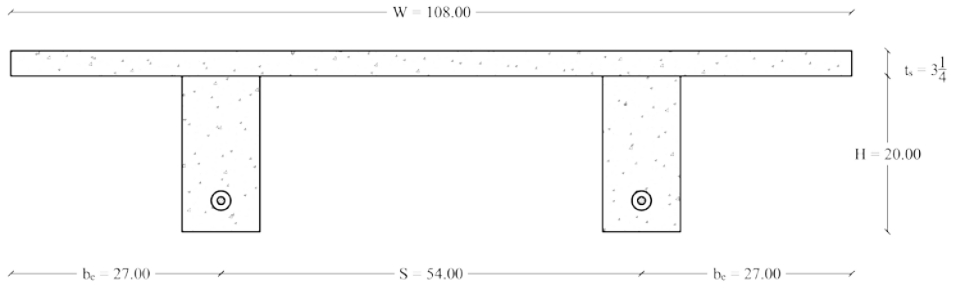

(*a*)

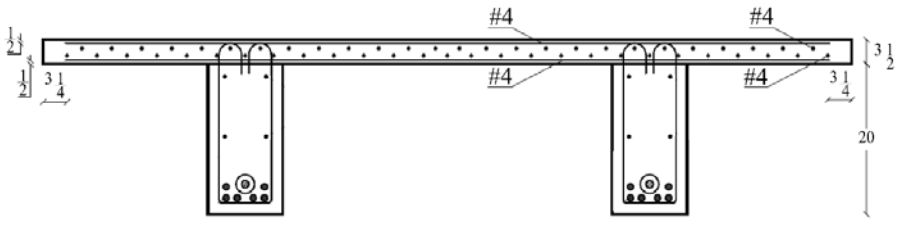

(*b*)

Figure 6.7: Cross-section dimensions (a) and rebars locations (b) for the deck section (all dimensions are in inches

(a)

(b)

Figure 6.8: RC deck before (a) and after (b) the concrete pour

To monitor the response of the structure during the testing, fourteen accelerometers were mounted to the bottom surface of the girder, and two additional accelerometer were installed on bottom surface of the deck. Two different types of Seismic ICP uniaxial piezoelectric accelerometers were used for this experiment: five model 393C, and four model 393B04 from PCB. Data was acquired through LabVIEW environment using four NI9234 modules with a sampling rate of 1652 Hz. Figure 6.9 shows the location of the sensors.

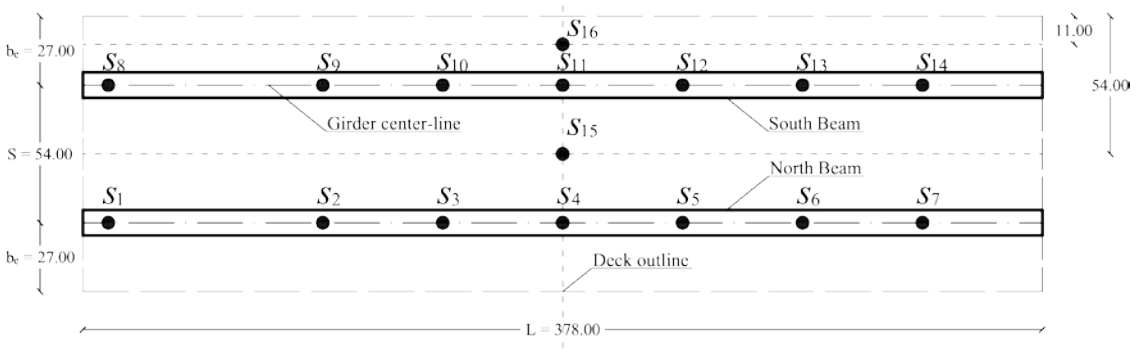

(*a*)

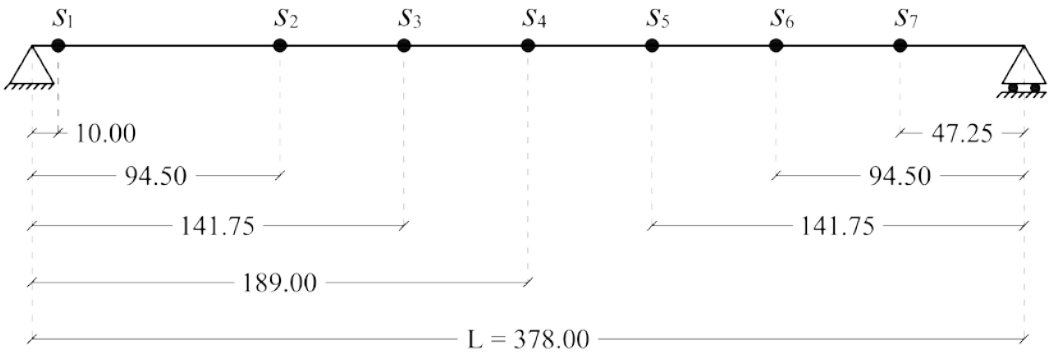

(*b*)

Figure 2.9: Sensors locations (a) top view and (b) side view (all dimensions in centimeters).

Figure 6.10: Testing of the system in undamaged condition

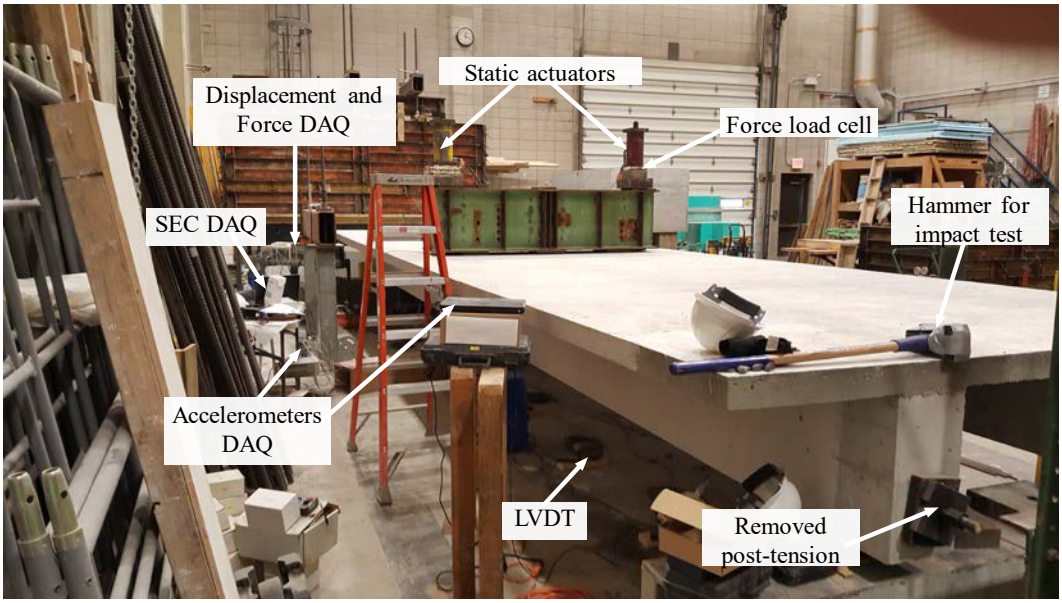

Figure 6.11: Experimental setup of double girder system.

Eighteen different damage cases were considered. Damage was induced in the girder using a pair of actuators mounted onto the top of the beam (Figure 6.11). These damage stages are characterized by the intensity of the load applied to the girders, summarized as follows:

- No damage: The system was analyzed before applying any load to it. Impact at different location were used to study the effect of load location and intensity on the identification process.
- Pre-compression removal: The pre-compression in the south beam was removed to ensure differential damage on the system during the remaining tests. The system was analyzed using 46 hammer impacts, applied in corresponded of the model nodes (girders mid-line). Three set of dynamic measurements were collected.
- Damage Case 1: The system was loaded with a load of at 26.6 kN (6 kips). Such load induced the formation of incipient damage at mid-span level in both girders.
- Damage Case 2: The system was loaded with a load of at 35.55 kN (8 kips). The additional load induced the formation of diffused cracks in the south beam, without any additional damage on the north beam.
- Damage Case 3: The system was loaded with a load of at 44.48 kN (10 kips).

- Damage Case 4: The system was loaded with a load of at - kN (12 kips).
- Damage Case 5: The system was loaded with a load of at - kN (18 kips).
- Damage Case 6: The system was loaded with a load of at - kN (24 kips).
- Damage Case 7: The system was loaded with a load of at - kN (30 kips).
- Damage Case 8: The system was loaded with a load of at - kN (36 kips).
- Damage Case 9: The system was loaded with a load of at - kN (42 kips).
- Damage Case 10: The system was loaded with a load of at - kN (48 kips).
- Damage Case 11: The system was loaded with a load of at - kN (54 kips).
- Damage Case 12: The system was loaded with a load of at - kN (60 kips).
- Damage Case 13: The system was loaded with a load of at - kN (70 kips).
- Damage Case 14: The system was loaded with a load of at - kN (80 kips).
- Damage Case 15: The system was loaded with a load of at - kN (90 kips).
- Damage Case 16: The system was loaded with a load of at - kN (100 kips).
- Damage Case 17: The system was loaded with a load of at - kN (120 kips).
- Damage Case 18: The system was loaded with a load of at - kN (130 kips).

CHAPTER 7: EXPERIMENTAL VALIDATION

The data collected from the experimental campaign were used to evaluate the performance of the proposed damage detection algorithm in dealing with realistic damage scenarios. The first test was focused on the evaluation of the performance at a component level. Using different damage scenarios the performance of the algorithm were evaluated both qualitatively and quantitatively, yielding good results in both fields. The second test was designed to provide a more challenging condition for damage identification, with a more complex system subjected to differential damage on the various components. Data from a multitude of damage cases were used to evaluate critical points of the proposed method. First, the detectability threshold of damage in the structure was assessed used data from incipient damage condition. Then, the capability to differentiate correctly and locate different levels of damage in different elements of the system was assessed. Finally, the accuracy of the quantitative evaluation was analyzed for damage conditions ranging from light, to severe and then critical.

7.1 Single PC girder – BTC60

As mentioned in chapter 6, the BTC60 was subjected to three different scenarios. The undamaged case was used to correct a simplified numerical model of the structure, achieving a good match from both the dynamical and statically point of view. The two subsequent damage cases were used to assess the performance of the damage detection algorithm using the previously generated model as a base reference.

7.1.1 No damage case

The tested beam was modeled in MATLAB as a two-dimensional structure, discretizing the beam into 36 elements of variable lengths (shown in Fig. 7.1) in order to account for sensor locations and the partial deck extensions. The beam was first divided based on sensors locations, and then a smaller element with length of 0.1778 m (7 in.) was defined to account for the offset of the deck in respect to the sensors S_2 and S_8. The remaining portions of the model were divided into smaller elements, with length ranging from 0.3302 m (13 in.) to 0.8382 m (33 in.), to achieve an accurate representation of the girder dynamics. Figure 7-1 presents the schematics of the discretized model, in which $F(t)$ indicates the force from the shaker. The properties of the MATLAB model are

estimated from the specimen's construction plans. This preliminary model is termed the non-updated model (NUM).

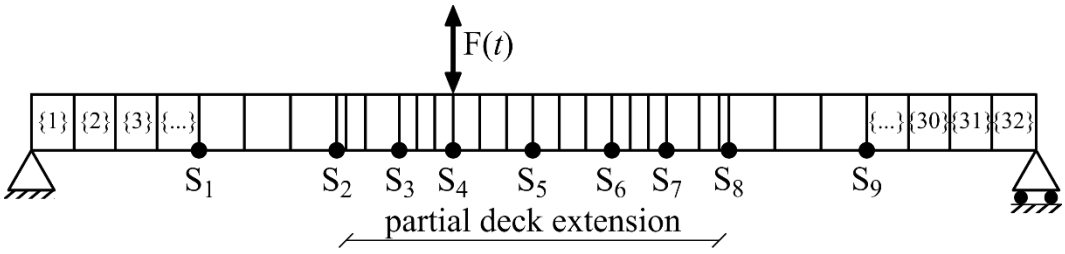

Figure 7.1: Finite element model discretization for the BTE60 girder

The model was then updated using the measured structural responses. Measured data were first filtered using a Chebyshev Type II low-pass filter to eliminate high frequency components of noise in the data, and then analyzed using the SSID algorithm to retrieve the dynamic properties of the specimen. Unlike for the numerical simulation, the retrieved modal properties differed significantly from the NUM. This is attributed to the differences between the beam as-designed and as-constructed. Hence, it is necessary to update the NUM to obtain the best match between the model and the data. This is done by allowing the modification of the stiffness and mass terms of the elements by a factor ranging from 0.8 to 1.2. The damage indices, α_i, were modified to include the variation in the stiffness and mass for each element, resulting in new indices denoted by β_i and γ_I representing the change in stiffness constants and masses, respectively. The optimization functions (i.e, Equations 4-2, 4-3 and 4-6) were then solved using the PSO, yielding a new model termed updated model (UM). Table 7.1 compares the retrieved frequencies from the SSID algorithm, with the frequencies from the NUM and the UM. A comparison of the errors shows that the UM resulted in a significant improvement in the modal parameters, reducing the maximum error on the frequencies from 4.30% to 1.82%. Figure 7.2(a) and 7.2(b) visually represent the modification factors for each element stiffness and mass, respectively.

Table 7.1: First three frequencies of the system retrieved with the SSID compared with the ones from the NUM and the UM

ode	SSID frequencies (Hz)	NUM frequencies (Hz)	NUM. error (%)	UM frequencies (Hz)	UM. error (%)
1	7.06	6.92	1.96	7.04	0.28
2	25.09	25.91	-3.30	24.98	0.40
3	56.15	58.59	-4.30	57.17	-1.82

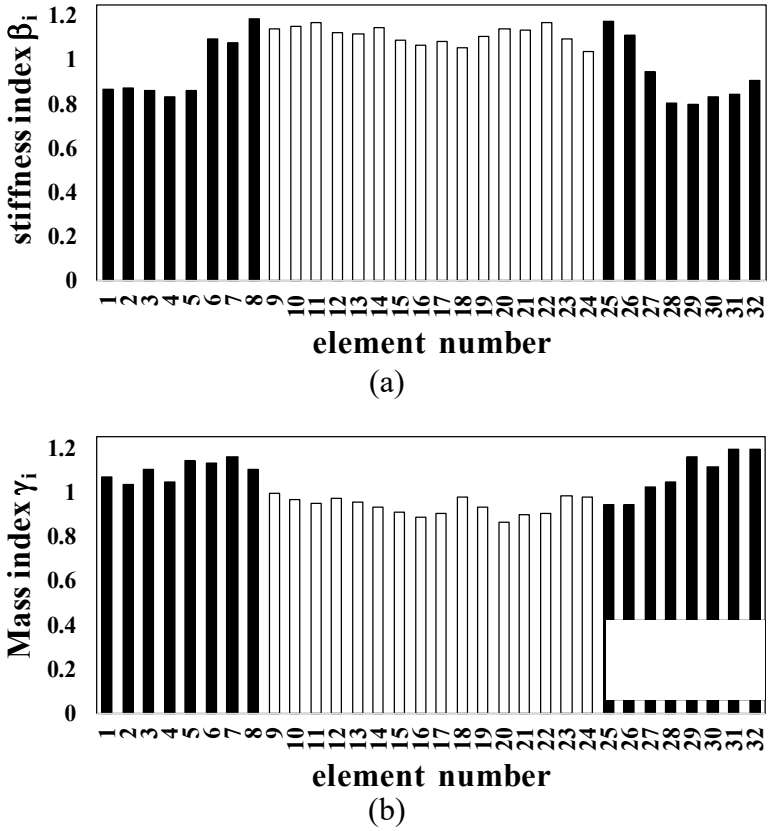

Figure 7.2: Modification factors (a) β_i for element stiffness and (b) γ_i for element mass.

The resulting model was further validated by comparing the static displacement measurements acquired from string potentiometers during the application of a static load of 178 kN (40 kips) applied at the center of the beam. Figures 7.3 compares the static displacement obtained from the NUM, the UM, and experimental data. Results show better agreement between the UM and the experimental data, with a deflection error at mid-span reducing from 5.1% to 0.2%. However, fitting errors persist on the right side of the system with no significant reduction after

the updating. This residual error may be attributed to an unmodeled variability in the boundary conditions, for instance from the chain used to secure the beam, and to the limited and localized excitation produced by the shaker that was located on the left-hand-side of the beam.

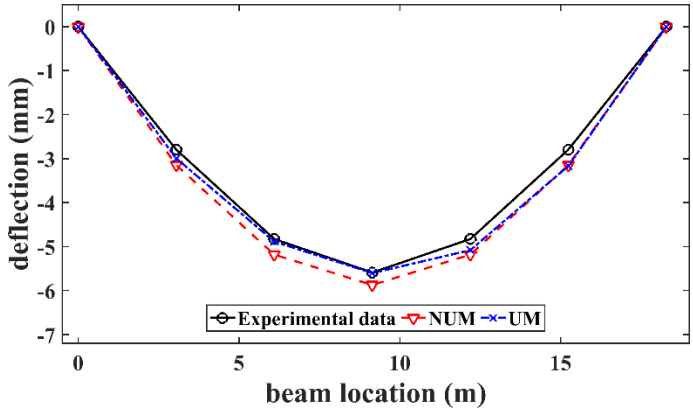

Figure 7.3: Comparison of the static deflection shapes.

7.1.2 Damage case 1

The same data processing methodology was applied to damage case 1. The first three frequencies of the specimen are compared with the no damage case in Table 7.2. It can be observed that all the frequencies decreased following the introduction of damage, with the third frequency being the most sensible to damage.

Table 7.2: Changes in frequencies due to damage case 1

mode	no damage frequencies (Hz)	damage 1 frequencies (Hz)	frequency change (%)
1	7.09	7.00	-1.27
2	25.03	24.97	-0.23
3	57.15	53.49	-6.40

Here, the UM is used as a reference model, and is updated to localize and quantify damage. However, only the element stiffness is modified, as it is assumed that mass remained constant. Figure 7.4 shows the damage indices obtained from this process. Their values represent the fraction of bending rigidity, *EI*, for each element relative to the reference model. Results show that only the elements under the deck area were damaged. This was consistent with the observations during the experiments, as shown in Figure 7.5 where cracks were visually observed. This updated model is termed updated model – damage 1 (UMD1).

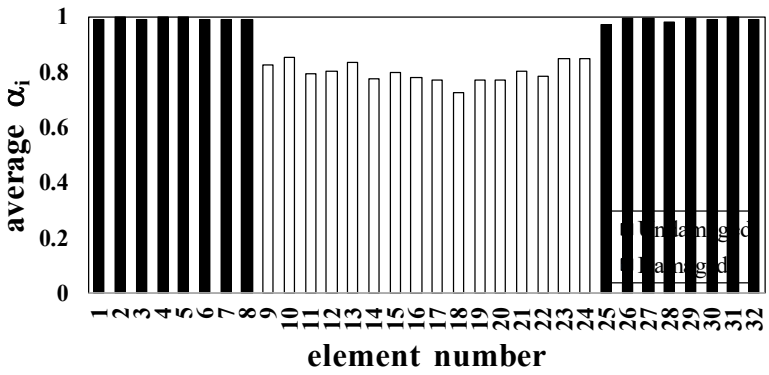

Figure 7.4: Average damage index for damage case 1

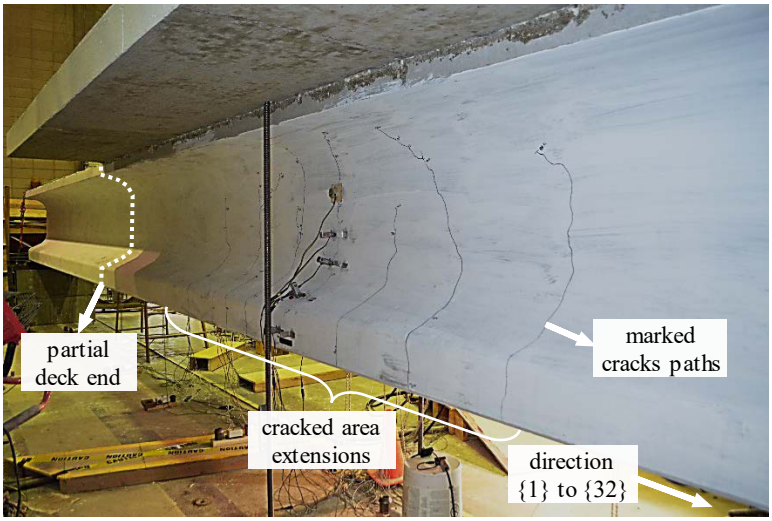

(a)

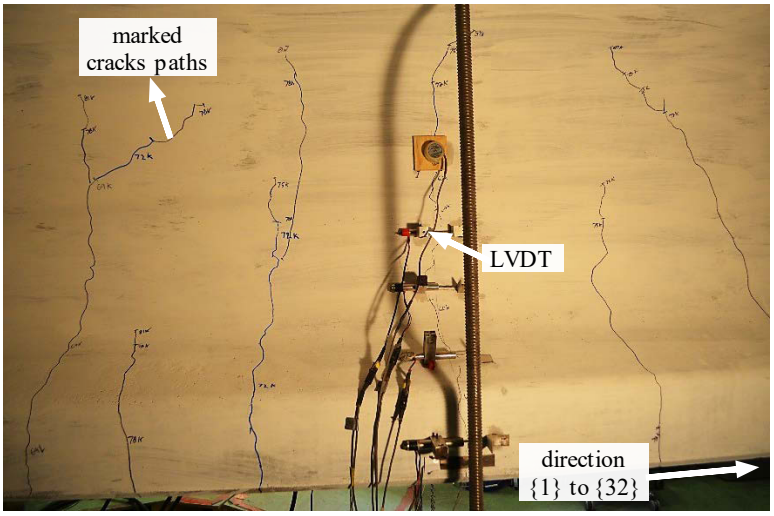

(b)

Figure 7.5: Crack pattern on BTC60 specimen under damage 1 condition.

7.1.3 Damage case 2

Similar to damage case 1, Table 7.3 lists and compares the first three frequencies retrieved through SSID. Once again, the third frequency shows a higher response to damage.

Table 7.3: Changes in frequencies due to damage case 2

mode	damage 1 frequencies (Hz)	damage 2 frequencies (Hz)	frequency change (%)
1	7.00	6.78	-3.14
2	24.97	24.65	-1.28
3	53.49	51.27	-4.15

Here, the UMD1 becomes the reference model for the damage detection process. This implies that the damage indices represent a further reduction in the elements' bending rigidity from the previous analysis. Figure 7.6(a) illustrates the retrieved damage indices, while Figure 7.6(b) plots the total average damage indices, α_i^*, that are relative to the UM. Results shows that some deterioration starts to appear outside of the deck area, but the majority of the damage is still concentrated under the deck area. This is supported by visual observations during the test. Figure 7.7 is a picture of the crack pattern under damage case 2.

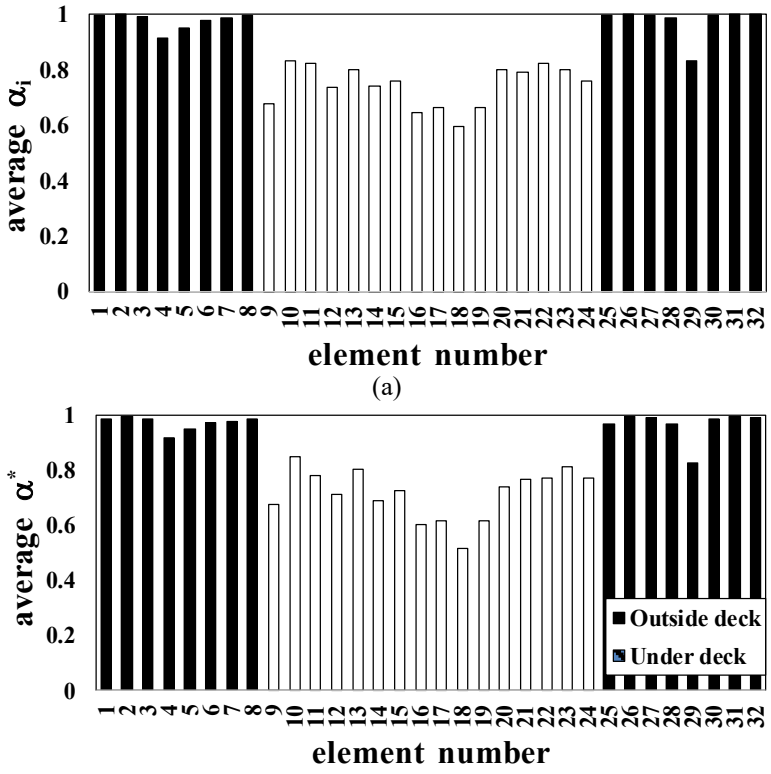

Figure 7.6: Damage indices for damage case 2 (a) relative average indices and (b) total average indices

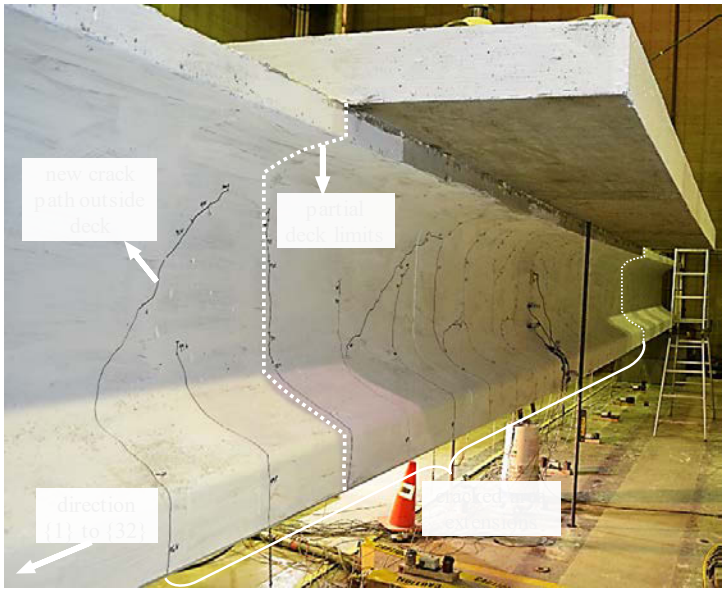

Figure 7.7: Crack pattern on BTC60 specimen under damage case 2

Lastly, the secant stiffness is used to further validate the model. The secant stiffness from the model is obtained by applying a unitary force at midspan and dividing the value by the midspan deflection $x_{\text{mid.}}$ The experimental reloading stiffness was taken as the tangent of the reloading curve, obtained from the data collected using a linear variable differential transformer (LVDT). The resulting model secant stiffness is 24826 kN/m (142 kips/in), while the experimental secant stiffness is 25227 kN/m (144 kip/in), a difference of 1.19 %, demonstrating a good match between the model and experimental data. This result demonstrates that the quantification of damages from the algorithm was likely accurate. Note that due to a malfunction of the LVDT, the experimental secant stiffness could not be computed under damage case 1.

CHAPTER 8: APPLICATION OF BAYESIAN UPDATING METHODS

One of the major challenge in any damage detection algorithm that employs a base mathematical model is non-uniqueness of the obtained solution. This may occur due to various uncertainties associated with mathematical model, uncertainty in boundary conditions, material properties, and modeling order. In addition to this, noisy and incomplete measurements also make it difficult to make the damage detection in a structure as a globally identifiable problem. The non-uniqueness of obtained solution here implies that there are more than one set of unknown model parameters (for example damage indices) that minimize the objective function to almost the same extent. In other words, more than one set of unknown model parameters are capable to generate the measured system output. This chapter deals with this problem by employing Bayesian framework for damage detection in bridge structures. The efficiency of the adopted Bayesian framework is illustrated employing a few numerical example from previous chapter.

8.1 Bayesian framework and Bridges health monitoring

In last few decades, the non-uniqueness issue has gained attention from many researchers and emerged as an important domain, associated with damage detection or model updating problems. This domain is widely accepted as model parameter uncertainty quantification. Among a few probabilistic approaches to deal with this uncertainty in model parameters, the globally accepted approach is Bayesian model updating. Bayesian model updating is a technique to deal with the damage detection or model updating problem in a probabilistic way to quantify the uncertainty in the unknown model parameters. In addition, it is also capable to take into account any prior information available about model parameters. In structural system identification, it was first introduced by Katafygiotis & Beck, 1998. A lot of work has been done in this area using both modal parameters and time history data of the [47]–[49]. Particular emphasis is placed on localizing and quantifying the existing damage in the structure [50]–[52]. A real life rail-cum-roadway long steel truss bridge (Saraighat bridge) is considered by Mustafa et al., 2015 for health monitoring and damage detection under Bayesian framework. Bayesian Bridge Condition Assessment (BBCA) method is developed by Dirbaz, 2013, which updates the damage index of a bridge structural component (a parameter to describe the extent of damage) under Bayesian inference. In a few other studies, a long-span cable-stayed bridge (using long-term monitoring data) [55], footbridge [56], several-span steel plate girder bridge with Gerber system [57] were

considered for health monitoring with Bayesian inference. Long-term health monitoring of bridge structures under Bayesian framework is considered by [57]. Their approach comprises of both Bayesian regression and Bayesian hypothesis testing to detect the structural changes in an in-service seven-span steel plate girder bridge with Gerber system. The analysis includes both temperature and vehicle weight effects in health assessment of the bridge. Damage detection in reinforced concrete bridge of the Egnatia Odos motorway under Bayesian framework is reported by Ntotsios et al., 2009. For damage localization they adopted a Bayesian model selection framework. Damage quantification is then achieved as the posterior probability of the model parameters derived for the most probable model class.

This work provides a modal data sensitivity-based Bayesian algorithm for health monitoring and damage detection in reinforced concrete bridge structures. Most of the available Bayesian algorithms treat all the major structural parameters as unknown and evaluate those using measured data from the structure. In large structures like bridges, the treatment of all parameters as unknown forces the identification problem to deal with a very high dimensional space. This makes the Bayesian algorithm computationally inefficient. Furthermore, if all measurements are not reliably acquired (which is often the case) or if higher modes of the structure are not properly evaluated, the accuracy of the algorithms may suffer. However, if the intact structure can be determined within permissible error limits using the as-built structural design/drawings or other available information, the dimensionality of the Bayesian problem can be reduced. This can be achieved by first localizing the damaged elements and then treating only these elements as unknown in the algorithm. This work utilizes a fundamental mode shape and its derivative based approach for the damage localization in the bridge prior to damage quantification. It is illustrated through a few numerical examples that accuracy and efficiency of the Bayesian algorithm can be improved significantly by localizing the damage in the bridge prior to its quantification.

8.2 Bayesian model updating with modal data

The need to predict the response of a physical system due to a future excitation involves the requirement of a correct mathematical model for that system. A mathematical formulation for a physical problem involves the understanding of the basic physical laws associated with the problem, associated material properties and then representing those in the language of mathematics. However, a true behavior of a structural system can only be understood by studying

its response under applied loads. In Bayesian model updating the parameters of a system that define its mathematical model are updated using the response of the system itself so that a more reliable mathematical model of the system can be achieved. The updating is assumed to be satisfactory when the response of the mathematical model matches with the response of the physical system for a given input. The following relation is a primary relation for any Bayesian model updating scheme, employing the following relation Bayes' theorem can be written with three distinct terms.

$$Posterior\ distribution \propto\ Likelihood \times Prior\ distribution$$

The three terms of the above relation comprise the whole process of the probabilistic mathematical model updating scheme starting from any prior knowledge about the model parameters to obtain the current status of the model parameters incorporating the all available experimental/real time outcome of the process. Prior distribution for any model parameter is determined based on the available knowledge about the parameter. The term likelihood is a probabilistic function which relates the plausibility of getting the observed outcome of the process for a given value of parameter of the mathematical model. Finally, the term posterior distribution gives a more favorable distribution for the unknown model parameters. Mathematically the above relation can be written as:

$$p(\theta \mid D) = \frac{p(D \mid \theta) p(\theta)}{p(D)} \tag{8-1}$$

where, $\theta \in R^n$ is the parameter vector which need to be updated and D is the available data from the system. Expression $p(\theta)$ is known as the prior distribution of parameter vector θ and $p(D \mid \theta)$ represents the probability of the data D when a belief of θ is taken as true. The term $p(D \mid \theta)$ is called as the likelihood of data, D, for that belief. The total probability of the data, D, for the model is a constant. This can be given by the sum of the likelihood of data D for each and every belief of θ i.e. $\sum_{i=1}^{n} p(D \mid \theta_i)$ and is represented as $p(D)$. The expression $p(\theta \mid D)$ is called as the posterior distribution of the parameter vector θ. If data D consists of modal data of the system, it can be shown that likelihood for frequency and mode shape components can be expressed as:

$$p(\omega_i / \boldsymbol{\theta}, \sigma_{\omega_i}) = \frac{1}{\sigma_{\omega_i}\sqrt{2\pi}} e^{-\frac{(\omega_i - \bar{\omega}_i(\boldsymbol{\theta}))^2}{2\sigma_{\omega_i}^{\ 2}}} \tag{8-2}$$

$$p(\boldsymbol{\varphi}_i / \boldsymbol{\theta}, \mathbf{V}_{\boldsymbol{\varphi}_i}) = \frac{1}{(2\pi)^{n/2} \mathbf{V}_{\boldsymbol{\varphi}_i}^{1/2}} \exp\left(-\frac{1}{2} \left(\boldsymbol{\varphi}_i - \hat{\boldsymbol{\varphi}}_i(\boldsymbol{\theta})\right)^T \mathbf{V}_{\boldsymbol{\varphi}_i}^{-1} \left(\boldsymbol{\varphi}_i - \hat{\boldsymbol{\varphi}}_i(\boldsymbol{\theta})\right) \right) \tag{8-3}$$

where, ω_i and $\boldsymbol{\varphi}_i$ represent the observed frequency and the mode shape vector of the i^{th} mode of the system $i = 1...m$. Frequency and mode shape of the mathematical model for the i^{th} mode are represented as $\hat{\omega}_i(\boldsymbol{\theta})$ and $\hat{\boldsymbol{\varphi}}_i(\boldsymbol{\theta})$, respectively. The likelihood formation for frequency and mode shape components is done assuming that the deviation between the system and model output is a normal distribution. In other words, the prediction error models for the used data points are assumed to be normally distributed with some standard deviation or variance. Standard deviation of the deviation in frequency of the i^{th} mode is taken as σ_{ω_i}. Whereas, $\mathbf{V}_{\boldsymbol{\varphi}_i}$ represents the covariance matrix of the deviation in i^{th} mode shape vector components. Further, it is assumed that the frequency and mode shape of an energy mode are statically independent informatively. Now, if each mode is also assumed independent to other mode then for m modes the likelihood of the evidence D can be given as:

$$p(D / \boldsymbol{\theta}) = \prod_{i=1}^{m} p\left(\omega_i \mid \boldsymbol{\theta}, \sigma_{\omega_i}\right) . p\left(\boldsymbol{\varphi}_i \mid \boldsymbol{\theta}, \mathbf{V}_{\boldsymbol{\varphi}_i}\right) \tag{8-4}$$

To evaluate the covariance matrix, $\mathbf{V}_{\boldsymbol{\varphi}_i}$, in the above equation, mode shape components are taken as uncorrelated to each other. As a result, $\mathbf{V}_{\boldsymbol{\varphi}_i}$, comes to be a diagonal matrix. Now, if, d is the length of the parameter vector θ, then the total unknown parameters in updating problem increase to $d + m(n+1)$, where, n is the number of observed degrees of freedom. The unknown parameter vector θ thus becomes:

$$\bar{\boldsymbol{\theta}} = \left\{ \boldsymbol{\theta}^T, \left\{ \sigma_{\omega_i}^2, \mathbf{V}_{\boldsymbol{\varphi}_i 11} ... \mathbf{V}_{\boldsymbol{\varphi}_i nn} \right\}_{i=1}^{m} \right\}^T \tag{8-5}$$

Equation (8-4) now can be rewritten as:

$$p(D / \bar{\boldsymbol{\theta}}) = \prod_{i=1}^{m} p\left(\omega_i \mid \bar{\boldsymbol{\theta}}\right) \prod_{j=1}^{n} p\left(\boldsymbol{\varphi}_{ij} \mid \bar{\boldsymbol{\theta}}\right) \tag{8-6}$$

In Equation 8-6, considering all variances as unknown makes the updating algorithm inefficient due to the increased dimensionality of the problem. Therefore, this project exploits the

modal data sensitivity towards structural parameters to evaluate these variances [59]. This approach results in obtaining exhaustive information from the data used for the updating without increasing the number of unknown parameters (unknown variances for each data point) in the updating algorithm.

For this purpose, vector S is considered which consists of absolute change in each and every modal data element used for updating due to a small change in structural parameters and is normalized with respect to its maximum element. Then, the normalized vector S can be adopted as the normalized variances of prediction error models of different modal data points. The logic behind this adoption is that a relatively lower change in a modal data with a change in structural parameters enforces a relatively narrow error span and in turn, a relatively lower variance for prediction error model of this modal data. The same reason can be given for adopting a relatively higher variance for prediction error model of a data point with relatively higher sensitivity. Therefore, using these normalized variances all unknown variances can be obtained in updating algorithm by considering only one unknown (σ) and the probability of D (Equation 8-6) now becomes:

$$p(D/\boldsymbol{\theta}) = \prod_{i=1}^{m} p\left(\omega_i \mid \boldsymbol{\theta}, c_{i+(i-1)n}.\sigma^2\right) \prod_{j=1}^{n} p\left(\varphi_{ij} \mid \boldsymbol{\theta}, c_{i+j+(i-1)n}.\sigma^2\right) \tag{8-7}$$

where c_i with $i = 1...m\ (1 + n)$ is the i^{th} element of the normalized vector S and can be evaluated as below:

$$c_{\omega_k} = \frac{s_k^{\omega}}{max(\mathbf{s})}; \qquad c_{\phi_{kp}} = \frac{s_{kp}^{\phi}}{max(\mathbf{s})} \tag{8-8}$$

Furthermore, s_k^{ω} and s_{kp}^{ϕ} can be given as:

$$s_k^{\omega} = \sum_{i=1}^{d} \left| \frac{\dfrac{\Delta_i \hat{\omega}_k^j}{\hat{\omega}_k^j}}{\Delta\theta_i^j} \right| \qquad k = 1, 2, ...m \tag{8-9}$$

$$s_{kp}^{\phi} = \sum_{i=1}^{d} \left| \frac{\dfrac{\Delta_i \hat{\phi}_{kp}^{j}}{\hat{\phi}_{kp}^{j}}}{\Delta \theta_i^{j}} \right| \qquad \text{for } k = 1,2,...m; \text{ and } p = 1,2,..n \tag{8-10}$$

where, $\Delta_i \hat{\omega}_k^j$ and $\Delta_i \hat{\phi}_{kp}^j$ represent the change in $\hat{\omega}_k^j$ and $\hat{\phi}_{kp}^j$, respectively, due to a small change in θ_i^j.

8.3 Numerical illustration

For the numerical illustration of the approach, the single RC girder as described in Chapter 5 is employed. Both the scenarios of damage (damage in two consecutive elements 7 and 8 in Scenario I and damage in elements 9 and 13 in Scenario II) are considered. Damage indices, α_i, for all the elements are taken as unknown and evaluated under Bayesian inference. First three modes data are used to determine the unknown parameters under Bayesian inference. These modal data are contaminated by noise of coefficient of variation 5% and 2% to represent the high and low noise contamination cases, respectively. A total of 15 such contaminated data sets are then taken in each noise case to determine the unknown damage indices. To avoid any bias in the algorithm exponential prior with mean value of 2 which is very far from the actual value of damage indices is adopted for the choice of prior distribution. Gamma distribution is adopted as the proposed distribution for all the unknown parameters. Metropolis-Hasting Markov Chain Monte Carlo (MCMC) simulation algorithm is employed to draw samples from the high dimensional posterior distribution.

Results for both the damage scenarios and both noise cases are shown in Tables 8.1 and 8.2. These tables present the mean and variance of the posterior distributions of the unknown damage indices. Deviations of mean of posterior distributions of unknown damage indices from their actual values is also presented in these tables. It can be observed from these tables that for both the damage scenarios and noise cases the deviation is quite less for most of the unknown damage indices. The uncertainty associated with the resolution of an unknown parameter can be observed in terms of the associated variance of that parameter as shown in Tables 8.1 and 8.2. As expected the associated uncertainty reduces with the good quality data (less noisy) employed for the quantification.

It can also be observed form Tables 8.1 and 8.2 that taking damage indices for all damaged and undamaged elements as unknowns can lead to higher errors in some of the unknown parameters (for example 13.32% and 35.27% in element 16 for damage scenario I and II, respectively). This is particularly true for high noise contamination case. The reason behind this is the insufficient data used (only three modes) for the updating or damage quantification. In other words, the employed data for damage quantification do not carry sufficient information to resolve all the unknown parameters. Furthermore, in case of higher noise levels in the employed data the updating problem may become globally unidentifiable. It is observed that the problem can be resolved by increasing the number of modes in the employed data for updating. However, obtaining the all higher modes experimentally for real structures like bridges is another challenging task. One solution for this problem can be obtained by localizing the damage in the structure before quantification using methods such as those discussed in earlier chapters of this report. If the intact structure's properties can be determined with reasonable accuracy, then all the undamaged elements can be taken as known in the algorithm. Employing this as an accurate and efficient quantification method can be achieved for the known locations of damage. Following section describes a mode shape and its derivative based approach proposed by Roy & Ray-Chaudhuri [60] for the damage localization in the beam girder.

8.4 Mode shape based damage localization

From literature [61]–[63] it is evident that damage in a structure can be localized by comparing its damaged and undamaged mode shapes and their derivatives proposed a mathematical basis to establish a correlation between structural damage and change in the structure's fundamental mode shape and its derivatives using a perturbation approach [60].

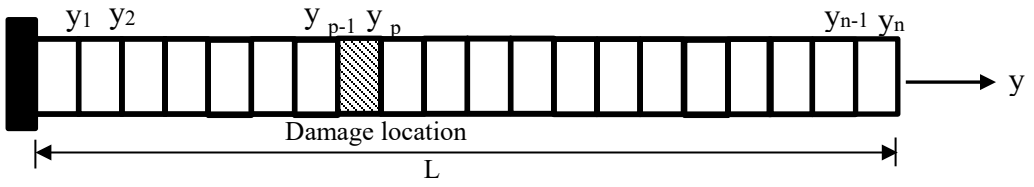

Figure 8.1: Schematic diagram of a shear beam

For a shear beam (Figure 8.1) they illustrated that the difference between the damaged and undamaged fundamental mode shapes can be expressed as:

$$\partial\phi(y_l)=\begin{cases}\mu\left[\dfrac{\pi}{2}-f(y_l)\right]: & y_l > y_p \\ \mu\left[\dfrac{\pi}{4}-f(y_l)\right]: & y_l = y_p \quad ; \; l=1...n \\ \mu\left[-f(y_l)\right]: & y_l < y_p \end{cases} \tag{8-11}$$

where, μ is a constant as given in [60] and $f(y_l)$ is given by:

$$f(y_l)=2\sin\left(\frac{\pi y_l}{2L}\right)\cos\left(\frac{\pi y_p}{2L}\right) \tag{8-12}$$

Table 8.1: Bayesian damage quantification for damage scenario I without localization

Unknown parameters with actual value	5% noise case			2% noise case		
	Mean	Variance	Absolute deviation (%)	Mean	Variance	Absolute deviation (%)
α_1=1.0	0.92	0.0077	7.75	1.02	0.0016	1.65
α_2=1.0	1.00	0.0014	0.44	1.05	0.0001	4.89
α_3=1.0	0.99	0.0011	0.76	1.04	0.0000	3.85
α_4=1.0	0.99	0.0005	0.71	1.04	0.0001	4.45
α_5=1.0	0.91	0.0011	8.82	1.06	0.0001	6.12
α_6=1.0	0.98	0.0018	2.22	1.03	0.0003	3.35
α_7=0.8	**0.80**	**0.0007**	**0.05**	**0.80**	**0.0000**	**0.41**
α_8=0.7	**0.72**	**0.0004**	**2.64**	**0.71**	**0.0000**	**1.73**
α_9=0.7	1.06	0.0008	6.06	1.03	0.0001	3.30
α_{10}=1.0	1.02	0.0010	1.77	0.99	0.0003	1.43
α_{11}=1.0	0.88	0.0015	12.18	1.08	0.0003	7.69
α_{12}=1.0	1.00	0.0018	0.16	1.06	0.0001	5.58
α_{13}=0.8	0.98	0.0015	1.77	1.06	0.0001	5.63
α_{14}=1.0	0.97	0.0006	2.91	1.03	0.0000	3.14
α_{15}=1.0	0.99	0.0005	1.21	1.06	0.0004	5.63
α_{16}=1.0	1.13	0.0093	13.32	1.02	0.0024	1.67

Table 8.2: Bayesian damage quantification for damage scenario II without localization

Unknown parameters with actual value	5% noise case			2% noise case		
	Mean	Variance	Absolute deviation (%)	Mean	Variance	Absolute deviation (%)
α_1=1.0	0.92	0.0057	7.52	1.07	0.0015	6.66
α_2=1.0	0.98	0.0009	1.64	0.95	0.0000	4.63
α_3=1.0	1.02	0.0001	1.51	0.99	0.0001	0.82
α_4=1.0	0.97	0.0005	3.36	0.97	0.0001	3.49
α_5=1.0	0.94	0.0010	6.05	0.98	0.0003	2.15
α_6=1.0	0.95	0.0020	4.64	0.95	0.0002	5.43
α_7=1.0	1.05	0.0034	4.71	1.03	0.0002	3.09
α_8=1.0	0.98	0.0019	2.11	0.98	0.0001	1.97
α_9=0.7	**0.75**	**0.0005**	**6.61**	**0.71**	**0.0000**	**0.76**
α_{10}=1.0	1.01	0.0011	0.62	1.02	0.0001	1.66
α_{11}=1.0	0.92	0.0012	8.14	0.97	0.0002	3.15
α_{12}=1.0	0.98	0.0018	2.13	0.95	0.0003	5.38
α_{13}=0.8	**0.79**	**0.0004**	**1.01**	**0.78**	**0.0001**	**2.48**
v_{14}=1.0	0.97	0.0007	2.95	0.98	0.0002	2.32
v_{15}=1.0	0.96	0.0006	3.53	1.00	0.0001	0.17
v_{16}=1.0	1.35	0.0210	35.27	0.93	0.0013	6.66

It can be observed from Equation (8-7) that at $y_l = y_p$ (location of damage), the function $\partial\phi(y_l)$ has a steep slope owing to the jump of $\frac{\mu\pi}{2}$ between $y_l = y_{p-1}$ and $y_l = y_{p+1}$. Additionally, the second derivative of $\partial\phi(y_l)$ — $\partial\phi''(y_l)$ —changes its sign at $y_l = y_p$. Therefore, a damaged location can be identified with a zero crossing in the plot showing the change in mode shape curvatures due to damage.

This mode shape based approach is adopted to localize damage in the beam girder before Bayesian quantification for providing an efficient damage detection methodology. After damage localization, in Bayesian quantification algorithm damage indices of only damaged members are taken as unknown. All other damage indices are taken as known and equal to one. Figure 8.2 shows the plot of change in fundamental mode shape curvature of the beam due to damage for both the damage scenarios. As discussed earlier the damaged elements can be identified as the locations of zero crossing from this figure. For damage scenario II (Figure 8.2) the locations of zero crossing can be clearly identified at elements 9 and 13 which are the actual damaged elements for this

scenario. For damage scenario I (Figure 8.2), since damage is in two adjacent elements (7 and 8) the region of zero crossing is distributed among both of the elements. However, the damaged elements are clearly identifiable for this scenario also.

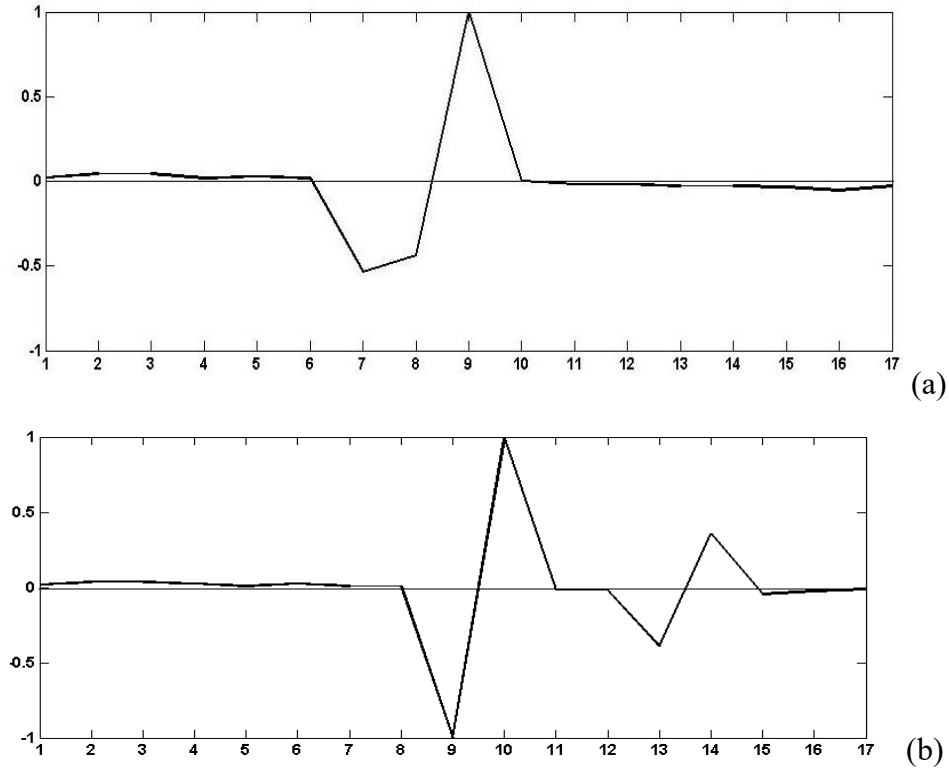

Figure 8.2: Change in fundamental mode shape curvature of the beam (a) damage Scenario I (b) damage scenario II

Tables 8.3 and 8.4 show the Bayesian quantification results for the localized damaged elements for both damage scenarios. It can be seen from Tables 8.3 and 8.4 that for both the damage scenarios and both the noise cases the deviations are within 5% range. It is also observed that the computational time also reduced significantly when localization is achieved prior to quantification. Markov chains for the two unknown damage indices are shown in Figure 8.3 for both the noise cases for damage scenario II. It can be observed form this figure that convergence of the chain near the actual value of unknown parameters is obtained just after a few runs of the chain. Figure 8.4 shows the posterior distributions of unknown damage indices for damage scenario II under both noise cases. The first 50 states of chain are shown in red in Figure 8.4. These states show the evolution of chains before reaching their stationary distribution. In literature these states are often referred as burn-in length of the chain and are discarded while evaluating the posterior distribution

of the unknown parameters. In this project also the posterior statistics is evaluated only after discarding the burn-in length of the chain. The actual posterior samples that are used to evaluate posterior statistical parameters are shown in black in Figure 8.4.

If results from the approach proposed in the previous chapter and the Bayesian approach proposed in this chapter are compared, then it can be observed that for the considered damage scenarios both the approaches are capable to provide good estimate of unknown parameters. However, one drawback of the approach provided in previous chapter over Bayesian approach is that in the former all three objective functions are considered independently to evaluate the unknown parameters. These resulted in different evaluation of the unknown parameters for each objective function. However, the final evaluation of unknown parameters is done combining all three results from independently solved objective functions with very simple strategy which is not grounded on firm logics. This may lead to erroneous results for more complicated damaged patterns in the bridge, and moreover, with insufficient and highly noise-contaminated vibrational data. On the other hand, proposed Bayesian framework provides a way to combine different available data or the based objective function (for example objective functions based on frequency and mode shapes) in a more meaningful and logical way. Therefore, it can be expected that the proposed Bayesian framework is more reliable for evaluating damage in bridges under more complex damage patterns and with insufficient and noise-contaminated vibrational data.

Table 8.3: Bayesian damage quantification for damage scenario I after localization

Unknown parameters with actual value	5% noise case			2% noise case		
	Mean	Variance	Absolute deviation (%)	Mean	Variance	Absolute deviation (%)
α_7=0.8	0.81	1.70E-03	1.24	0.79	8.00E-05	1.60
α_8=0.7	0.71	3.00E-04	1.89	0.68	4.00E-05	2.57

Table 8.4: Bayesian damage quantification results for damage scenario II after localization

Unknown parameters with actual value	5% noise case			2% noise case		
	Mean	Variance	Absolute deviation (%)	Mean	Variance	Absolute deviation (%)
α_9=0.7	0.71	3.00E-04	1.24	0.70	5.00E-05	0.63
α_{13}=0.8	0.83	4.00E-04	4.35	0.81	1.00E-05	0.82

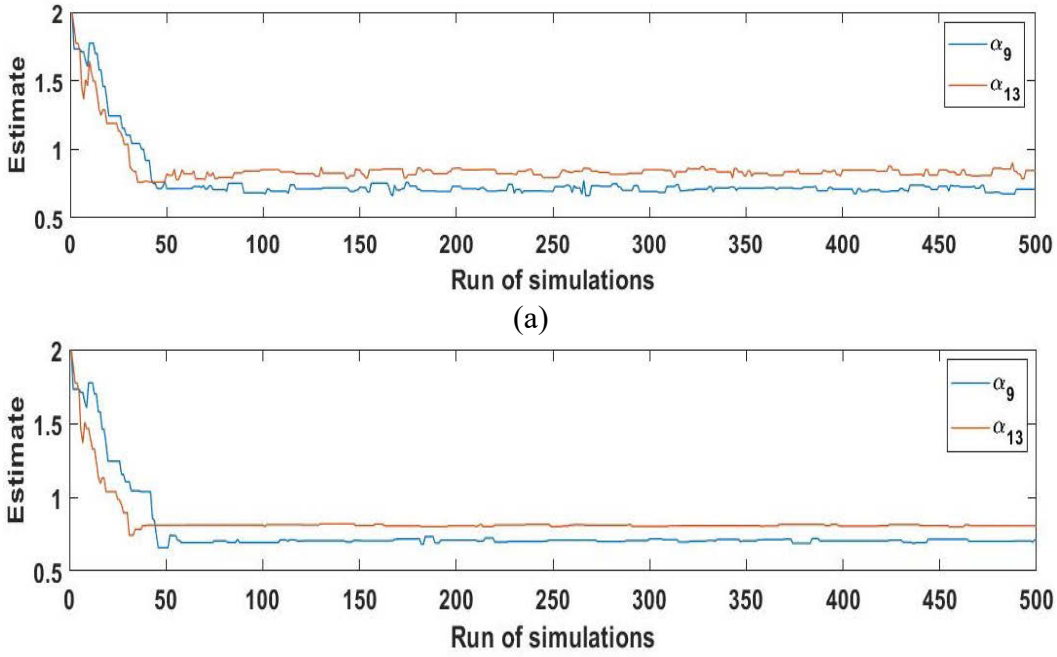

(a)

(b)

Figure 6.3: Markov chain for (a): 5% noise case (b): 2% noise case

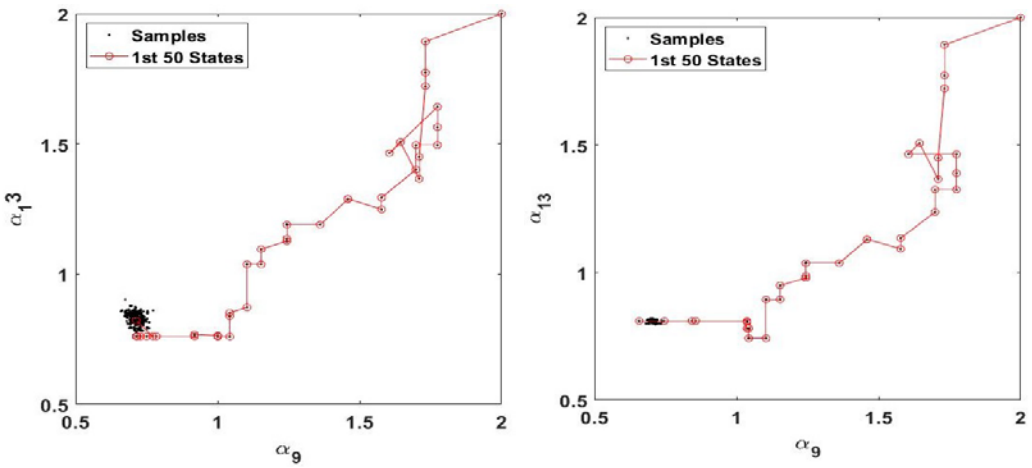

(a) (b)

Figure 6.4: Posterior distribution for damage scenario II (a): 5% noise case (b): 2% noise case

The results show that Bayesian framework is an effective and efficient approach for health monitoring of RC structures. It is concluded that localization of damaged elements prior to damage quantification can improve the damage quantification results significantly in terms of both accuracy and computational efficiency. For damage localization well-establish mode shape and its

derivative based approach is employed. Damage quantification is achieved using a modal data sensitivity based Bayesian approach. Efficiency of the proposed approach is illustrated employing numerical simulation of a RC beam girder. It can be concluded that the proposed can effectively detect and quantify damage under various damage scenarios in a RC beam girder.

CHAPTER 9: CONCLUSIONS AND FUTURE WORK

Decision frameworks that include a rational approach for quantifying the deterioration state and the associated uncertainties will offer a meaningful bridge management tool as it can reliably predict the future operation conditions of bridges. Robust structural health monitoring data, when available, provide a good platform to characterize the deterioration state and the associated uncertainties, enabling more realistic prediction of the structural performance bridges throughout their life cycle. The most common approach include the deployment of accelerometers that would make recordings of the structural response under both extreme and service loads. Historically California Department of Transportation (Caltrans) has been one of the leading state Departments of Transportation in deploying sensing instruments including accelerometers and tilt meters, in addition to an array of weather related instruments (e.g., anemometers) on bridges throughout the state. Although the original intent of this instrumentation was to monitor the performance of bridges during and after seismic events (in addition to other extreme events such as windstorms and floods), the added benefit of this wealth of data is to monitor the performance of the bridge under service loads and estimate its operational state with due consideration deterioration.

One of the major issues to be considered for long term monitoring of the bridges is that it is difficult to measure the input excitation on bridges, as they are excited by ambient/natural sources such as traffic, wind, micro-tremors, and combinations thereof. Thus, in most of the cases, it is required to extract the modal parameters from the structural response. As such, output-only techniques become a desirable approach for the damage identification of the structure. A few practical advantages of such methods over other methods are: i) there is no need to interrupt traffic to conduct controlled tests, ii) the in-situ dynamic behavior of the bridge under its normal operational conditions are captured, and iii) they can be conducted continuously, triggered automatically, or manually. As such, this project aimed to use a Bayesian based output only method that incorporates a priori knowledge, derived either from established theories, engineering experience, or FE based models into a probabilistic model of the structure system. Such a holistic SHM and structural damage identification and localization technique, will allow for estimation of the remaining life capacity (in operational conditions) as well as the safety the structure (after extreme events) or in other words a detailed Level IV identification scheme for the California bridges.

This project includes the following steps: 1) development of a robust diagnosis technique for the anomaly detection from the monitoring data for both extreme event rapid damage assessment as well as life-cycle operational anomalies resulting from deterioration and minor damages, 2) Choose two suitable experimental set ups in collaboration with Caltrans engineers to deploy the validated long-term continuous monitoring system model-based advanced data analysis, and 3) generate an advanced prognosis framework based on fundamentals of Bayesian updating to quantify the remaining life capacity of the structure.

This project presented a novel technique for damage detection, localization and quantification from vibration data. The method consists of 1) retrieving modal properties through an SSID algorithm; 2) reconstructing a reduced order stiffness matrix through the SEREP technique; and 3) reconstructing an FEM optimized with a PSO. By identifying the localization and quantities of altered mass and stiffness values necessary to update the FEM, the PSO was directly used for damage localization and quantification. The proposed approach was first verified on the numerical simulation of a simply supported reinforced concrete beam. Results showed that the algorithm was capable of detecting, localizing and quantifying damage with good accuracy under different scenarios. After, the methodology was validated on data collected from a full-scale bridge girder. The experiment utilized a pretensioned concrete girder excited with a white noise load using a hydraulic shaker, under the following three different damage scenarios: 1) undamaged; 2) damage case 1, pre-yielding; and damage case 2, post-yielding. Results from the undamaged specimen showed that it is possible to reconstruct a model that accurately reproduced the modal properties of the structure. Results from the damage cases demonstrated the capability of the algorithm to accurately update the FEM to identify the location of damages, supported by the visual observation of crack locations during the test. It is concluded that the algorithm demonstrated promise in producing an accurate FEM of the monitored structure using output-only data. Such model could be used to conduct numerical analyzes furthering the assessment of the structural condition.

The non-uniqueness of the solution may occur due to various uncertainties associated with mathematical model, uncertainty in boundary conditions, material properties, and modeling order. In addition to this, noisy and incomplete measurements also make it difficult to make the damage detection in a structure as a globally identifiable problem. The non-uniqueness of obtained solution here implies that there are more than one set of unknown model parameters (for example damage

indices) that minimize the objective function to almost the same extent. To address issues that may come up with non-uniqueness of solutions in the developed damage identification model, a Bayesian approach is utilized. The results show that Bayesian framework is an effective and efficient approach for health monitoring of RC structures. It is concluded that localization of damaged elements prior to damage quantification can improve the damage quantification results significantly in terms of both accuracy and computational efficiency. For damage localization well-establish mode shape and its derivative based approach is employed. Damage quantification is achieved using a modal data sensitivity based Bayesian approach. Efficiency of the proposed approach is illustrated employing numerical simulation of a RC beam girder. It can be concluded that the proposed can effectively detect and quantify damage under various damage scenarios in a RC beam girder.

With advancements in damage diagnosis, localization and prognosis through an integrated probabilistic approach, the completed project has paved the ground for development and implementation of a framework for the performance evaluation of structures using condition assessment methodologies that will lead to providing better estimates of the condition state of the structures used in life cycle planning activities.

REFERENCES

[1] T. Miwa, T. Kaihara, and Y. Nonaka, "Integrated Maintenance System Trend and a Maintenance Scheduling System Application," in *Through-life Engineering Services*, Springer, 2015, pp. 241–268.

[2] C. Liu, Y. Gong, S. Laflamme, B. Phares, and S. Sarkar, "Bridge damage detection using spatiotemporal patterns extracted from dense sensor network," *Meas. Sci. Technol.*, vol. 28, no. 1, p. 14011, 2016.

[3] V. Chinde, L. Cao, U. Vaidya, and S. Laflamme, "Damage detection on mesosurfaces using distributed sensor network and spectral diffusion maps," *Meas. Sci. Technol.*, vol. 27, no. 4, p. 45110, 2016.

[4] C. R. Farrar *et al.*, "Dynamic characterization and damage detection in the I-40 bridge over the Rio Grande," 1994.

[5] A. Downey, F. Ubertini, and S. Laflamme, "Algorithm for damage detection in wind turbine blades using a hybrid dense sensor network with feature level data fusion," *J. Wind Eng. Ind. Aerodyn.*, vol. 168, pp. 288–296, 2017.

[6] F. Ubertini, A. L. Materazzi, A. D'Alessandro, and S. Laflamme, "Natural frequencies identification of a reinforced concrete beam using carbon nanotube cement-based sensors," *Eng. Struct.*, vol. 60, pp. 265–275, 2014.

[7] T. J. Wipf, B. M. Phares, L. F. Greimann, D. L. Wood, and J. D. Doornink, "Evaluation of steel bridges (volume I): monitoring the structural condition of fracture-critical bridges using fiber optic technology," 2007.

[8] J.-T. Kim and N. Stubbs, "Nondestructive crack detection algorithm for full-scale bridges," *J. Struct. Eng.*, vol. 129, no. 10, pp. 1358–1366, 2003.

[9] C. Liu, J. T. DeWolf, and J.-H. Kim, "Development of a baseline for structural health monitoring for a curved post-tensioned concrete box-girder bridge," *Eng. Struct.*, vol. 31, no. 12, pp. 3107–3115, 2009.

[10] S. W. Doebling, F. M. Hemez, L. D. Peterson, and C. Farhat, "Improved damage location accuracy using strain energy-based mode selection criteria," *AIAA J.*, vol. 35, no. 4, pp. 693–699, 1997.

[11] F. Ubertini, G. Comanducci, and N. Cavalagli, "Vibration-based structural health monitoring of a historic bell-tower using output-only measurements and multivariate statistical analysis," *Struct. Heal. Monit.*, vol. 15, no. 4, pp. 438–457, 2016.

[12] J.-T. Kim and N. Stubbs, “Improved damage identification method based on modal information,” *J. Sound Vib.*, vol. 252, no. 2, pp. 223–238, 2002.

[13] A. Yan and J.-C. Golinval, “Structural damage localization by combining flexibility and stiffness methods,” *Eng. Struct.*, vol. 27, no. 12, pp. 1752–1761, 2005.

[14] A. Alipour, “Post-Extreme Event Damage Assessment and Response for Highway Bridges.” 2016.

[15] I. A. Nhamage, R. H. Lopez, and L. F. F. Miguel, “An improved hybrid optimization algorithm for vibration based-damage detection,” *Adv. Eng. Softw.*, vol. 93, pp. 47–64, 2016.

[16] E. Reynders, “System identification methods for (operational) modal analysis: review and comparison,” *Arch. Comput. Methods Eng.*, vol. 19, no. 1, pp. 51–124, 2012.

[17] C. Rainieri and G. Fabbrocino, “Automated output-only dynamic identification of civil engineering structures,” *Mech. Syst. Signal Process.*, vol. 24, no. 3, pp. 678–695, 2010.

[18] P. Andersen, R. Brincker, M. Goursat, and L. Mevel, “Automated modal parameter estimation for operational modal analysis of large systems,” in *Proceedings of the 2nd international operational modal analysis conference*, 2007, vol. 1, pp. 299–308.

[19] F. Magalhaes, A. Cunha, and E. Caetano, “Online automatic identification of the modal parameters of a long span arch bridge,” *Mech. Syst. Signal Process.*, vol. 23, no. 2, pp. 316–329, 2009.

[20] F. Ubertini, C. Gentile, and A. L. Materazzi, “Automated modal identification in operational conditions and its application to bridges,” *Eng. Struct.*, vol. 46, pp. 264–278, 2013.

[21] E. Neu, F. Janser, A. A. Khatibi, and A. C. Orifici, “Fully automated operational modal analysis using multi-stage clustering,” *Mech. Syst. Signal Process.*, vol. 84, pp. 308–323, 2017.

[22] B. Peeters, “System identification and damage detection in civil engeneering,” Katholieke Universiteit te Leuven, 2000.

[23] B. Peeters, G. De Roeck, T. Pollet, and L. Schueremans, “Stochastic subspace techniques applied to parameter identification of civil engineering structures,” in *New Advances in Modal Synthesis of Large Structure*.

[24] B. Peeters and G. De Roeck, “Reference-based stochastic subspace identification for

output-only modal analysis," *Mech. Syst. Signal Process.*, vol. 13, no. 6, pp. 855–878, 1999.

[25] E. Reynders and G. De Roeck, "Reference-based combined deterministic--stochastic subspace identification for experimental and operational modal analysis," *Mech. Syst. Signal Process.*, vol. 22, no. 3, pp. 617–637, 2008.

[26] L. Mevel, M. Goursat, and M. Basseville, "Stochastic subspace-based structural identification and damage detection and localisation—application to the Z24 bridge benchmark," *Mech. Syst. Signal Process.*, vol. 17, no. 1, pp. 143–151, 2003.

[27] J.-B. Bodeux and J.-C. Golinval, "Modal identification and damage detection using the data-driven stochastic subspace and ARMAV methods," *Mech. Syst. Signal Process.*, vol. 17, no. 1, pp. 83–89, 2003.

[28] A. C. Altun\i\cs\ik, F. Y. Okur, and V. Kahya, "Modal parameter identification and vibration based damage detection of a multiple cracked cantilever beam," *Eng. Fail. Anal.*, vol. 79, pp. 154–170, 2017.

[29] B. Peeters, J. Maeck, and G. De Roeck, "Vibration-based damage detection in civil engineering: excitation sources and temperature effects," *Smart Mater. Struct.*, vol. 10, no. 3, p. 518, 2001.

[30] J. Kullaa, "Damage detection of the Z24 bridge using control charts," *Mech. Syst. Signal Process.*, vol. 17, no. 1, pp. 163–170, 2003.

[31] W.-C. Su, C.-S. Huang, H.-C. Lien, and Q.-T. Le, "Identifying the stiffness parameters of a structure using a subspace approach and the Gram--Schmidt process in a wavelet domain," *Adv. Mech. Eng.*, vol. 9, no. 7, pp. 1–13, 2017.

[32] H. M. Gomes and N. R. S. Silva, "Some comparisons for damage detection on structures using genetic algorithms and modal sensitivity method," *Appl. Math. Model.*, vol. 32, no. 11, pp. 2216–2232, 2008.

[33] Z. Wei, J. Liu, and Z. Lu, "Structural damage detection using improved particle swarm optimization," *Inverse Probl. Sci. Eng.*, pp. 1–19, 2017.

[34] L. F. F. Miguel, R. H. Lopez, and L. F. F. Miguel, "A hybrid approach for damage detection of structures under operational conditions," *J. Sound Vib.*, vol. 332, no. 18, pp. 4241–4260, 2013.

[35] S. Moradi, P. Razi, and L. Fatahi, "On the application of bees algorithm to the problem of crack detection of beam-type structures," *Comput. Struct.*, vol. 89, no. 23, pp. 2169–2175,

2011.

[36] F. Kang, J. Li, and Q. Xu, “Damage detection based on improved particle swarm optimization using vibration data,” *Appl. Soft Comput.*, vol. 12, no. 8, pp. 2329–2335, 2012.

[37] C. M. Escobar, O. A. González-Estrada, and H. G. S. Acevedo, “Damage detection in a unidimensional truss using the firefly optimization algorithm and finite elements,” *arXiv Prepr. arXiv1706.04449*, 2017.

[38] X.-S. Yang, “Firefly Algorithm, Lévy Flights and Global Optimization,” in *Research and Development in Intelligent Systems {XXVI}*, Springer London, 2009, pp. 209–218.

[39] O. Begambre and J. E. Laier, “A hybrid Particle Swarm Optimization – Simplex algorithm (PSOS) for structural damage identification,” *Adv. Eng. Softw.*, vol. 40, no. 9, pp. 883–891, 2009.

[40] M. T. V. Baghmisheh, M. Peimani, M. H. Sadeghi, M. M. Ettefagh, and A. F. Tabrizi, “A hybrid particle swarm–Nelder–Mead optimization method for crack detection in cantilever beams,” *Appl. Soft Comput.*, vol. 12, no. 8, pp. 2217–2226, 2012.

[41] V. Meruane and W. Heylen, “Damage detection with parallel genetic algorithms and operational modes,” *Struct. Heal. Monit.*, vol. 9, no. 6, pp. 481–496, 2010.

[42] S. Z. Rad, “Methods for updating numerical models in structural dynamics,” Department of Mechanical Engineering, Imperial College, 1997.

[43] J. Kennedy and R. Eberhart, “Particle swarm optimization,” in *Neural Networks, 1995. Proceedings., IEEE International Conference on*, 1995, vol. 4, pp. 1942–1948 vol.4.

[44] G. Venter and J. Sobieszczanski-Sobieski, “Particle swarm optimization,” *AIAA J.*, vol. 41, no. 8, pp. 1583–1589, 2003.

[45] J. Connor and S. Laflamme, *Structural motion engineering*, vol. 9783319062. 2014.

[46] L. S. Katafygiotis and J. L. Beck, “Updating Models and Their Uncertainties. II: Model Identifiability,” *J. Eng. Mech.*, vol. 124, no. 4, pp. 463–467, 1998.

[47] J. L. Beck and S.-K. Au, “Bayesian Updating of Structural Models and Reliability using Markov Chain Monte Carlo Simulation,” *J. Eng. Mech.*, vol. 128, no. 4, pp. 380–391, 2002.

[48] L. Mthembu, T. Marwala, and M. I. Friswell, “Bayesian Evidence for Finite Element

Model Updating," in *Proceedings of IMAC XXVII: A Conference & Exposition on Structural Dynamics*, 2009, pp. 1–10.

[49] R. Astroza, H. Ebrahimian, Y. Li, and J. P. Conte, "Bayesian Nonlinear Structural FE model and Seismic Input Identification for Damage Assessment of Civil Structures," *Mech. Syst. Signal Process.*, vol. 93, pp. 661–687, 2017.

[50] K. Prajapat and S. Ray-Chaudhuri, "Damage Detection in Railway Truss Bridges Employing Data Sensitivity under Bayesian Framework: A Numerical Investigation," *Shock Vib.*, vol. 2017, 2017.

[51] M. W. Vanik, J. L. Beck, and S. K. Au, "Bayesian Probabilistic Approach to Structural Health Monitoring," *J. Eng. Mech.*, vol. 126, no. 7, pp. 738–745, 2000.

[52] M. Kurata, J. P. Lynch, K. H. Law, and L. W. Salvino, "Bayesian Model Updating Approach for Systematic Damage Detection of Plate-Type Structures," *Conf. Proc. Soc. Exp. Mech. Ser.*, vol. 4, pp. 85–94, 2012.

[53] S. Mustafa, N. Debnath, and A. Dutta, "Bayesian Probabilistic Approach for Model Updating and Damage Detection for a Large Truss Bridge," *Int. J. Steel Struct.*, vol. 15, no. 2, pp. 473–485, 2015.

[54] M. Dirbaz, "A Bayesian Updatjng Approach in Structural Health Monitoring for Damage Detection and Assessment," 2013.

[55] P. Asadollahi, Y. Huang, and J. Li, "Bayesian Finite Element Model Updating and Assessment of Cable-Stayed Bridges using Wireless Sensor Data," *Sensors (Switzerland)*, vol. 18, no. 9, 2018.

[56] I. Behmanesh and B. Moaveni, "Probabilistic Identification of Simulated Damage on The Dowling Hall footbridge through Bayesian Finite Element Model Updating," *Struct. Control Heal. Monit.*, vol. 22, pp. 463–483, 2015.

[57] C. W. Kim, Y. Zhang, Z. Wang, Y. Oshima, and T. Morita, "Long-Term Bridge Health Monitoring and Performance Assessment Based on a Bayesian Approach," *Struct. Infrastruct. Eng.*, vol. 14, no. 7, pp. 883–894, 2018.

[58] E. Ntotsios, C. Papadimitriou, P. Panetsos, G. Karaiskos, K. Perros, and P. C. Perdikaris, "Bridge Health Monitoring System Based on Vibration Measurements," *Bull. Earthq. Eng.*, vol. 7, no. 2, pp. 469–483, 2009.

[59] K. Prajapat and S. Ray-Chaudhuri, "Prediction Error Variances in Bayesian Model Updating Employing Data Sensitivity," *J. Eng. Mech.*, vol. 142, no. 12, p. 04016096,

2016.

[60] K. Roy and S. Ray-Chaudhuri, “Fundamental Mode Shape and Its Derivatives in Structural Damage Localization,” *J. Sound Vib.*, vol. 332, no. 21, pp. 5584–5593, 2013.

[61] R. P. C. Sampaio, N. M. M. Maia, and J. M. M. Silva, “Damage Detection using The Frequency-Response-Function Curvature Method,” *J. Sound Vib.*, vol. 226, no. 5, pp. 1029–1042, 1999.

[62] H. Zhu, L. Li, and X. Q. He, “Damage Detection Method for Shear Buildings using The Changes in The First Mode Shape Slopes,” *Comput. Struct.*, vol. 89, no. 9–10, pp. 733–743, 2011.

[63] A. K. Pandey, M. Biswas, and M. M. Samman, “Damage Detection From Mode Changes In Curvature,” *J. Sound Vib.*, vol. 145, pp. 321–332, 1991.